ALMA MATER STUDIORUM · UNIVERSITÀ DI BOLOGNA

Scuola di Scienze
Corso di Laurea Magistrale in Fisica

Thermally reduced Graphene Oxide: a well promising way to transparent flexible electrodes.

Relatore:
Prof. Beatrice Fraboni

Correlatore:
Prof. Paolo Samorì

Presentata da:
Serena Morselli

Sessione III
Anno Accademico 2014/2015

A Mattia e alla mia Famiglia, sempre e comunque al mio fianco.

Contents

Abstract **iii**

Introduction **v**

1 Theoretical **2**

1.1 Graphene: history, properties and perspectives . . . 2
1.2 Processability limits of graphene and advantages of graphene oxide . . . 4
1.3 Reduction methods . . . 6
1.4 Transparent conductive films (TCFs) . . . 8
1.5 Flexible electronics . . . 9

2 Materials, methods and instruments **12**

2.1 Graphene Oxide . . . 12
2.2 Rhodamine 6G . . . 13
2.3 Deposition technique . . . 14
2.4 Annealing process . . . 15
2.5 Device fabrication . . . 17
2.6 Film transfer . . . 18
2.7 Atomic Force Microscopy . . . 19
  2.7.1 Contact mode AFM . . . 20
  2.7.2 Tapping mode AFM . . . 21
  2.7.3 Force spectroscopy . . . 22
  2.7.4 AFM tips . . . 23
2.8 X-rays Photoelectron Spectroscopy . . . 24
2.9 Electrical characterization . . . 27
  2.9.1 Sheet resistance . . . 28
  2.9.2 Gating effect . . . 29
2.10 UV-vis-NIR transmittance measurements . . . 29
2.11 UV-photoelectron spectroscopy . . . 31
2.12 ThermoGravimetric Analysis . . . 33

3 Experimental **36**
3.1 Film morphology through AFM characterization . . . 36
3.2 XPS analysis . . . 40
3.3 Sheet resistance . . . 42
3.4 Transmittance . . . 44
3.5 ThermoGravimetric Analysis . . . 46
3.6 UPS data analysis . . . 47
3.7 Electrical characterization . . . 49
3.8 Rhodamine 6G doping . . . 51
3.9 Mechanical characterization . . . 53

Conclusions **58**

Bibliography **62**

Abstract

La presente tesi studia la riduzione termica dell'ossido di grafene nell'ottica di una ottimizzazione del processo in termini di conducibilità elettrica e trasmittanza ottica, con lo scopo di ottenere parametri favorevoli alla creazione di elettrodi trasparenti e flessibili.

La riduzione termica è uno dei possibili metodi per ripristinare le proprietà elettriche originarie del grafene, compromesse dalla presenza dei gruppi ossidanti, i quali rompono i doppi legami C-C del reticolo a celle esagonali, ma in compenso rendono il materiale altamente idrofilo e trattabile in soluzione. Questo consente la deposizione di film di ossido di grafene tramite spin-coating, tecnica ottimale per la produzione di film uniformi e di spessore controllabile e riproducibile, e la successiva riduzione termica, effettuata variando i parametri chiave, ovvero temperatura e tempo di riduzione e velocità di riscaldamento, con l'obiettivo di ottimizzare il processo.

Il presente lavoro si compone di un capitolo introduttivo volto a presentare la storia del grafene, dalla sua scoperta alle prospettive applicative future, tra cui l'elettronica trasparente e flessibile, con un particolare focus sull'ossido di grafene come punto di partenza per garantire scalabilità industriale ed economicità del processo. A seguire, un capitolo su materiali, metodi e tecniche traccia una panoramica sui differenti set up sperimentali per la produzione dei campioni, la loro manipolazione e, in particolare, gli apparati utilizzati per effettuare la loro caratterizzazione, che sfrutta tecniche quali microscopia a forza atomica, spettroscopia UV e a raggi X, analisi termo-gravimetrica, spettrofotometria UV-vis-NIR. I dati ottenuti da queste misure sono, infine, presentati e discussi nel terzo capitolo, incentrato sugli aspetti sperimentali.

I risultati raggiunti sono promettenti. La deposizione via spin-coating produce film continui e uniformi in rugosità e spessore. Il processo di riduzione è stato ottimizzato in termini di sheet resistance e trasmittanza ottica, raggiungendo valori pari a, rispettivamente, (19±1)k$\Omega/\square$ e 82,9% a 550nm per un campione di pochi nanometri di spessore, a significare buona conduttività combinata con ottima trasparenza sull'intero range UV-vis-NIR. Questi risultati sono la conclusione di un processo di selezione di temperature e tempi di riduzione, oltre che di perfezionamento della fase di riscaldamento del campione, che si è avvalso di analisi XPS e termogravimetriche, oltre a misure di trasmittanza ottica e sheet resistance tramite metodo a quattro punte.

In termini di funzione lavoro, i film di grafen ossido ridotto termicamente mostrano una work function variabile a seconda del grado di riduzione, consentendo di spaziare su valori compresi tra i 5.0eV e i 5.4eV, con un trend orientato verso i valori del grafene per i film maggiormente ridotti. Questo dato è positivo perché, nel caso di integrazione del film in dispositivi richiedenti una specifica work function, si ha modo di selezionare quella più adeguata.

Per quanto riguarda l'estensiva caratterizzazione elettrica dei film sotto effetto di gate, si evince dalle curve I_dV_g un alto numero di difetti reticolari, i quali si traducono in mobilità ridotte per entrambi i portatori di carica e in uno shift positivo del Dirac gate voltage, punto in cui i portatori di carica passano da essere elettroni a lacune e viceversa, atteso a 0V. Effettuando, però, un drogaggio tramite Rodamina 6G, noto dopante di tipo n per il grafene, si ottiene un interessante shift negativo della curva, che porta il Dirac point a circa 10V e che può essere ulteriormente diminuito di 20V irradiando il campione alla frequenza di assorbimento della Rodamina 6G, in modo da indurre il trasferimento elettronico dalla Rodamina al film di grafen ossido ridotto. Questo trasferimento elettronico è alla base del meccanismo con cui il film effettua quenching della fluorescenza della Rodamina ed è reversibile solo mediante prolungato passaggio di corrente nel film. In sostanza, mostriamo come il drogaggio del film tramite Rodamina 6G si componga di due fasi successive, una per semplice deposizione, l'altra innescata dall'irradiazione, entrambe reversibili e di tipo n.

Infine, grazie al fatto di aver messo a punto una tecnica di trasferimento del film su substrati altrimenti inadatti perché patternati o non riscaldabili alle alte temperature della riduzione (come il PET), abbiamo potuto misurare le curve di carico del film sospeso su una micro-well tramite AFM e estrarre il modulo elastico 2D di pochi layers di grafen ossido ridotto, ottenendo valori dell'ordine di 10^3 N/m, superiori a quelli del grafene.

Introduction

The carbon atom is a fundamental building block in nature; the complexity of its chemical bonds is the main reason of its being at the origin of life. According to its degree of hybridization (sp, sp^2, and sp^3), it can assembly into different materials. Some of them have been known for a long time, such as natural graphite and diamond, but, particularly in the last half century, the researchers have uncovered many new materials. Graphite has been the first to be object of intense studies, after the identification of its structure in the beginning of the 20th century, and it followed a development of both theoretical and experimental aspects. In 1985, the discovery of fullerene started the era of nanocarbons, which, in the following years, included also nanotubes and graphene. In particular, the attention of the scientific world is now on graphene thanks to Geim and Novoselov of Manchester University, whose work presenting the isolation of monolayer graphene in 2004 and winning the Nobel Prize in Physics in 2010 can be considered the key event for the actual scientific and technological interest in graphene and graphene based materials.

Graphene, a two dimensional honeycomb lattice of carbon atoms, is known for its excellent electrical and mechanical properties, its thermal stability and for the particular feature of being a zero band gap semiconductor, with switchable charge carriers and very high mobility. Graphene has therefore an enormous potential in technological applications and the involved field can be several: from high frequency electronics to chemical sensors, touch panels, conductive ink, energy, and light emitting devices. The creation of new technologies based on graphene is subject to overcoming a variety of challenges and achieving several goals. Among these, the production of graphene is a very important aspect: we need to find reproducible, reliable, safe and sustainable large-scale production methods for graphene and related materials, according to the specific needs of different application areas.

The possible techniques for graphene production are many, from mechanical exfoliation of highly oriented pyrolitic graphite, to substrate based processes (epitaxial growth and chemical vapor deposition). One of the most promising path for a highly scalable, inexpensive production method is the reduction of the graphene oxide (GO) obtained by oxidation and exfoliation of graphite.

The present work is focused on the reduction of graphene oxide via thermal annealing, one of the several ways to perform the reduction. Thermal reduction is far more health and environmental safe than chemical reduction, because of the negligible side products. Moreover, thermal reduction gives the possibility to deal with graphene oxide in solution and reduce it after deposition. In fact, GO is highly dispersible in water because of the oxidizing groups, so that we can work with solutions instead of powders or isolated flakes for what concerns the formation of the film, and we proceed with the reduction only after the deposition. Depositing solutions is an optimal starting point to have uniform films of controllable thickness.

Our aim is to optimize the reduction process to obtain films that are not only conductive, but also transparent. For a set thickness, we can play with annealing time and temperature, and vary the heating ramp, so that optical transmittance and sheet resistance are optimized.

More in detail, after a theoretical introduction in Chapter 1, where the history of graphene, its declination as graphene oxide and relative advantages, and some perspectives concerning its applications in flexible electronics are presented, in Chapter 2 we illustrate the materials, the instrument we use, and the production techniques we follow. In particular we produce reduced graphene oxide (rGO) films on quartz for transmittance and sheet resistance measurements and on Si/SiO_2 substrates to build bottom-gate, top-contact field-effect transistors for electrical characterization under gate bias. We also optimize a transfer technique that enables the deposition of reduced films even on flexible substrates.

In Chapter 3 we illustrate the measurements we perform on the samples and we analyze the results. In particular, we characterize the rGO film morphologically via AFM and we examine the thickness of the film before and after reduction in search of a correlation between the two values. Thanks to sheet resistance and XPS spectra, we check the degree of reduction of the film and select the most promising range of reduction temperatures in terms of conductivity. The optical transmittance values, instead, are the key parameter to restrict the range of possible reduction times and give the start to an analysis of the influence of the heating ramp on the thinning of the film during reduction, mastered with ThermoGravimetric Analysis. From the UV-photoelectron spectroscopy data, we are able to individuate a trend of the rGO work function, according to the degree of reduction. Afterwards, we perform the electrical characterization of field-effect transistors, which gives indications on the quantity of defects in the lattice and is useful to analyze the doping effect of Rhodamine 6G on rGO films and the fluorescence quenching of the dye by the graphene. Finally, the transfer of the reduced films on patterned substrates allows us to measure the Young modulus of our film, using an Atomic Force Microscopy technique on rGO membranes suspended over micrometric wells.

Chapter 1

Theoretical

1.1 Graphene: history, properties and perspectives

Reduced graphene oxide (rGO), the material on which this work is focused on, is a graphene derivative resulting from the attempt of enhancing the processability and the large-scale production of graphene itself. In few pages, it will be clear why the choice of the material ended up on rGO, but in order to have a better understanding of its structure, properties, and the goals connected with the reduction process, it is important to introduce first its precursor the graphene.

Graphene is a structure made by sp^2-hybridized carbon atoms arranged into a two-dimensional sheet following a hexagonal lattice, the so-called honeycomb lattice. The stack of multiple graphene layers, hold together by Van der Waals interaction, gives rise to 3D graphite, while the roll up of a single flakes originates 1D carbon nanotubes and if the honeycomb lattice is arranged to form a spherical particle, we have 0D fullerene. The interest in graphene is due to the extraordinary thermal, electrical and mechanical properties that this carbon allotrope presents. The expectation of the theoretical studies have been confirmed in 2004 by Geim and Novoselov's work[1] that presented isolated single graphene flakes, confuting the hypothesis that such bi-dimensional crystals were thermodynamically stable only at infinitesimal temperatures.

The anisotropic structure of graphitic materials leads to interesting anisotropic properties. In particular, the s, p$_x$ and p$_y$ orbitals of each carbon atom are hybridized, forming covalent sp^2 bond that appear at 120°. Out of plane, instead, the remaining p$_z$ orbital, together with the three neighbor atoms, form a valence band of π orbitals and a conduction band of π* orbitals. The four electrons of each carbon atom contribute to form in-plane bonds (three electrons are employed for the σ bond and one for the π bond), therefore there are no more electrons to develop further chemical bonding in the c-direction. The out-of-plane interactions are then very weak, resulting in very low thermal and electrical conductivity in c-direction, three order of magnitude smaller than

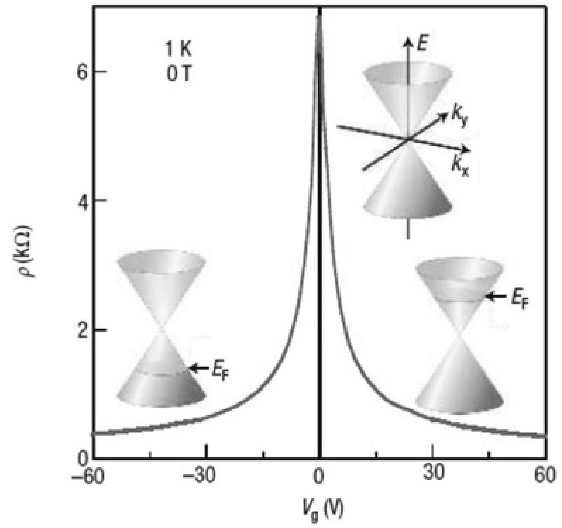

Figure 1.1: Graphene band structure with and without gating, and the consequent ambipolar electric field effect on the carriers. At zero voltage, valence and conduction band spontaneously meet at the single Dirac point. When a positive (negative) gate is applied, electrons (holes) are injected, inducing an enhancement of their mobility as result of the shift of the Fermi level (E_F).[3]

their in-plane analogous[2]. Because of this orbital structure, graphene flakes composed by few carbon layers show a metallic behavior, since some carrier wave functions overlap; the single-layer graphene flakes, instead, behave quite differently and are classified as zero band gap semiconductors (or semimetal). They present, in fact, a single Dirac point, which is the intersection of the highest occupied molecular orbital (HOMO) and the lowest occupied one (LUMO) (see Figure 1.1).

The main consequence of this electronic structure is ambipolarity: gating the graphene, the Fermi level, normally coincident with the Dirac point, can be shifted in the valence or conductive band, that is to say the carriers can be continuously tuned between holes and electrons, according to the gate applied. For non-zero gate, the electrical resistivity drops and the carriers gain a very high mobility up to 200000 $cm^2V^{-1}s^{-1}$ (single-layer, mechanically exfoliated, suspended graphene flake).[3] These high mobility values are due to the surprisingly low density of defects that normally inhibit charge transport, acting as scattering centers.[4]

The potential of development and engineering of this material is enormous and the idea of a new electronic is very tempting: by simply gating the graphene, doping levels become dynamically controllable and completely reversible, and the device can be easily reconfigured without any physical modification. Ambipolarity is an advantage also for the application of graphene as sensor. 2D materials are already a very favorable choice for sensing processes because of their maximal area to volume ratio: in layered materials, where there is no distinction between surface and bulk, every adsorption event on the surface affects as well the properties that are classified as bulk ones (such as resistivity). This is typical of bidimensional materials, and in graphene it is enriched by ambipolarity, thanks to which the adsorption of either electron-donating or withdrawing groups is possible and meaningful.[5] (See Figure 1.2)

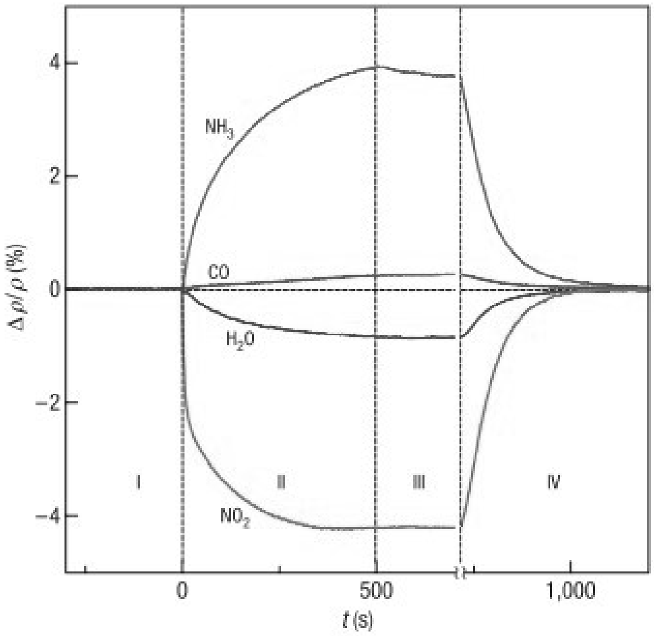

Figure 1.2: Sensitivity of graphene to chemical doping. Changes in resistivity, ρ, at zero B caused by graphene's exposure to various gases diluted in concentration to 1 p.p.m. The positive (negative) sign of changes is chosen here to indicate electron (hole) doping.[5]

1.2 Processability limits of graphene and advantages of graphene oxide

The fundamental premise for these extraordinary applications and results is the production of single-layer graphene. The methods are many and have been wisely improved, but any of them should possibly respond to three important requirements: the process should ensure fine control over the crystallite thickness, it should produce films with low density of defects to have high carrier mobility, and it should be industrially scalable.

The first successful approach to single-layer graphene production has been the micromechanical exfoliation method carried on by the Manchester group led by Geim.[1] The process to detach graphene from a graphite crystal (HOPG) consists in using adhesive tape, that at the first step removes multiple-layer graphene. To obtain few- or single-layer graphene, a repeated peeling is necessary, that also cleaves the graphene in flakes. Afterwards the tape is attached to the substrate and detached via glue solving. The last step is a peeling with an unused tape to further reduce the number of layers. Mechanical exfoliation is now optimized to yield high quality layers, with size up to the order of millimeters, limited only by the single crystal grains in the starting HOPG. Even if it is still the method of choice for fundamental studies, it is yet difficult to make it feasible for large-scale applications.

An alternative route that succeed in scalability is the graphene chemical vapor deposition (CVD) through hydrocarbons reacting with nickel or transition-metal-carbide surfaces. In fact the high temperature (over 1000°C) of the Si/SiO_2 substrate with a thin layer ($\sim$300nm) of nickel on it activates the adsorption of carbon on the substrate, and then the fast rate cooling to room temperature by argon flow suppresses the formation of multiple layers of graphene.[6]

Another substrate-based technique is the epitaxial growth, where silicon carbide is reduced at 1000°C in UHV leaving behind graphitized carbon islands.[7] The substrate and many growth parameters have a strong influence on the mechanical properties of the film grown with epitaxial growth or with CVD and for both of them, even if the scalability is potentially very good, the control of the thickness is still a difficult achievement.

To conclude this brief overview on the main production techniques of single-layer graphene, it is important to talk about the graphene oxide and its reduction. Graphene oxide is a graphene related material that presents the same layered, honeycomb-lattice structure and can be commercially found as a water dispersion. The main differences with the graphene are exactly its hydrophilicity, and the presence of many defects, as missing bonds inside the lattice or as oxygen-containing groups at the edges or in the basal plane, that inhibits charge transport and makes the GO flakes insulating. The origin of these extra groups bonded to the flake is their production method that start from oxidizing graphite. By Hummers method,[8] in fact, an aggressive chemical reaction, driven by a mixture of sulfuric acid, sodium nitrate and potassium permanganate, breaks the double carbon-carbon bonds of graphite and induces the intercalation of groups such as epoxy or hydroxyl ones between the layers. In this configuration, the layers of graphite are more spaced and easily separable (by sonication, stirring or thermal expansion for example) and the groups now decorating the single- or few-layers flakes make them much more hydrophilic. Their dispersion in pure water or aqueous mixture is easily achieved and this is of sure advantage to the formation of a thin film. Actually, many common techniques can be applied to deposit uniform and thickness-controlled films, such as spin coating, rod coating, spray coating, Langmuir-Blodgett technique, ink-jet printing, drop casting, dip casting and many others.[9]

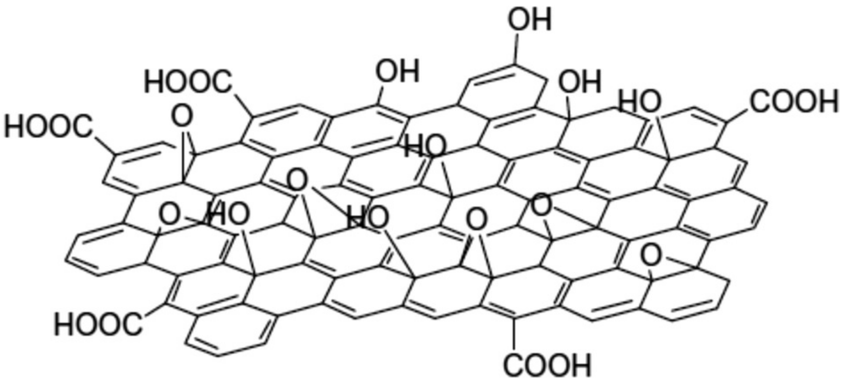

Figure 1.3: Structure of graphene oxide with epoxy and hydroxyl functional groups decorating the carbon plane and carboxylic groups on the periphery. Minor groups, as carbonyl, ester, etc. are omitted.[10]

1.3 Reduction methods

Graphene oxide is still a hot topic for what concerns the mass applications of graphene in particular and its development in general, even if the research has already elaborated few interesting methods for graphene production that guarantee excellent properties as a consequence of the relatively perfect structure of the products. Significant examples of these methods are epitaxial growth,[11 12 13] micro-mechanical exfoliation of highly ordered pyrolityc graphite[1], and CVD (chemical vapor deposition),[6 12 14] but in comparison to them, the GO methods still has two advantages for what concerns the aimed large-scale use of graphene: first, graphene oxide can be produced by inexpensive, high yield chemical methods that use as raw material cost-effective graphite; second, the high GO hydrophilicity allows to form stable aqueous colloids, facilitating the film formation processing the solution in cheap and simple ways. The graphene production process by GO is incomplete without the reduction step: the final product rGO presents restored conductive properties that depend upon the reduction process, which therefore affects the performances of the rGO-composed materials or devices. For this reason, the GO reduction is still a key topic that we will now investigate further.

The reduction processes for GO can be mainly classified in chemical methods, thermal methods or multistep ones, the latter including both chemical and thermal approaches. The chemical reduction, which is done in solution, is usually performed at room temperature or under moderate heating; therefore the equipment and the requirements for the environment are not as critical as in the thermal approaches. This makes generally the chemical approach cheaper and easily available for rGO mass production. Not surprisingly, the most common reduction method, that has been also one of the first to be reported, is the GO chemical reduction by hydrazine monohydrate. Differently from many other reductans, hydrazine monohydrate and its derivatives do not react with water, making them very attractive for reducing aqueous dispersions of GO. Adding the reductant to the dispersion upon 80°C to 100°C heating, a black solid precipitates because of the increased hydrophobicity of the material upon reduction. The black solid is in fact an agglomerate of graphene-based nanosheets that can be kept separated for an easy application by adding surfactants (soluble polymers) or ammonia. This method, very effective at removing oxygen functionality, has the relevant disadvantage of creating covalent bonds between nitrogen (in case of hydrazine and derivatives) and the graphene oxide surface. These residual C-N groups affect the electronic structure of the graphene, acting as n-type dopants.[15]

Other approaches that can be classified as chemical ones are Photo-catalytic reduction, Electrochemical reduction and Solvothermal reduction.[16]

Looking for a reductant-free method that can avoid undesired doping of the material, the thermal approach is an interesting alternative for reduction. The thermal process can be performed both on liquid solution of GO and on solid, pre-deposited films of material. In liquid, the annealing of the GO solution allows to exfoliate and reduce the material at the same time. Actually, the pressure of the CO and CO_2 gases evolved during the reduction is enough to separate single sheets of material, leading directly to graphene as final product. The flakes obtained in this way are however very small and wrinkled, because the decomposition of oxygen-containing groups during the reduction also removes carbon atoms from the carbon plane, for a total mass loss of c.a 30% and a final structure heavily damaged,[17 18] which affects the conductivity of the material. A partial solution to this problem is to separate the exfoliation and the reduction steps: large sized GO flakes can be produced by liquid phase exfoliation of graphite, then brought to solid phase (e.g. film or powder) and finally thermally reduced. The reduction is carried out in vacuum,[19] inert[20] or reducing atmosphere,[20 21] since residual oxygen has an etching effect on the material at high temperatures and the evolved gas can exert an exfoliating pressure on the film and a consequent loss of material. The choice between different atmospheres depends upon the set-up availability, the need of doping or not the material during the reduction and the maximal temperature available, since in case of H_2 atmosphere the reduction can be carried out at lower temperatures. Of course, the temperature is a key parameter for the good success of the thermal reduction, together with the heating speed and time. One of the indicators to classify the goodness of the reduction is the carbon-to-oxygen ratio (C/O ratio), obtained by XPS measurements or by elementary analysis measurements by combustion and goes from 4:1-2:1 in GO[22 23 24] to values generally around 12:1 in rGO,[24 25] but values of 246:1 have been recently reported.[26] For temperatures up to 500°C, the carbon/oxygen ratio is hardly bigger than 8:1, indicating that the conversion of C=O and O=C-OH groups into new chemical species is still incomplete, but it improves significantly at higher temperatures (700°C and 900°C), where the C/O ratio is higher than 13:1.[27] Obviously, thermal treatment is energy and time consuming and the range of possible substrates for the film deposition is limited by the high melting point requirement, but still the thermal reduction is a highly effective method, far more healt-safe than the chemical one.

An interesting combination of chemical and thermal approaches is the multistep method, where, for example, a first exposition to hydrazine vapor reduces the annealing temperature required to complete the reduction of the material.[28] This intuitively gives the possibility to use substrates with lower melting points, e.g. polymeric substrate, and the conductivity is comparable to that obtained for annealing at 550°C, but still does not reach the highest values reported in literature.[19 29]

1.4 Transparent conductive films (TCFs)

The reduced Graphene Oxide is one of the transparent conductive films (TCFs) of the new generation, which are fundamental for many technologies, such as LEDs, solar cells, liquid crystal displays, sensors and many others, and are developing in the direction of a higher economic affordability for mass scale production. Apart from high electrical conductivity and low absorption coefficient in the visible light range, another general important requirement for TCFs is thermal stability. TCFs are often subjected to high temperatures because of thermoelectric effect and, in some application, direct exposition to natural heat (e.g. solar cells). Lastly, good etchability is a very desirable feature for TCFs because allows to form patterns in the electrode. Presenting all these features, In_2O_3/Sn Indium Tin Oxide (ITO), is the milestone of the TCFs market. More in detail, it has high optical transmittance in the visible and near infrared region, higher than 80%,[30] and very low sheet resistance, down to 6 $\Omega/\square$.[31]

Due to the high costs of Indium, ITO is yet very expensive and many other materials are being investigated to find appropriate alternatives to it. An interesting alternative can be found among polymers: there are some conductive, organic polymers, which are also light weighted, inexpensive, flexible, and well compatible with plastic substrates. These polymers facilitate electron movement through their sp^2 hybridized backbone and their optimization led to very competitive conductivity: the most common among these polymers is PEDOT:PSS (poly(3,4-ethylenedioxythiophene) polystyrene sulfonate) and its sheet resistance is comparable to that of ITO for the same value of relative optical transmission, as may be seen in Figure 1.4.

In this challenge for an optimal and less expensive alternative to ITO, graphene obtained via GO reduction is a very interesting competitor. As shown in Figure 1.5, the rGO presents high and stable transmittance values over a wide range of wavelengths, while, even if ITO and FTO have higher transmittance values at short wavelengths, they are yet strongly absorbing in near- and short-wavelength IR region. Apart from conductivity, that is object of optimization according to the different reduction methods, the rGO presents also: excellent mechanical properties;[28] the possibility to form a pattern with laser reduction or by physical scratch; and, as shown later in this work: tunable work-function; morphological uniformity of the film; thermal stability; transferability

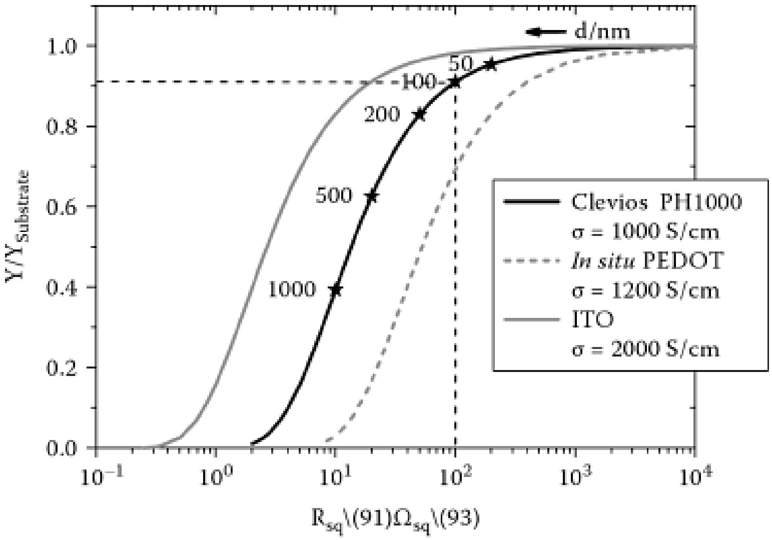

Figure 1.4: Relative optical transmission of ITO, PEDOT:PSS and in situ PEDOT versus sheet resistance. For PEDOT:PSS the thickness of the film d(nm) is indicated with the asterisks.[32]

onto flexible substrates as a trick to avoid problems connected with the melting points of the desired substrates.

1.5 Flexible electronics

The field of flexible electronics is wide and constantly developing. Flexible can mean many things: elastic, non-breakable, bendable, lightweight, permanently shaped or roll-to-roll manufacturable. The first approach to flexible electronics dates back to the 1960s. Thinning single crystal silicon wafer cells to ∼100 μm, Crabb and Treble[33] and, independently, Ray[34] made the first flexible solar cell arrays, in which the flexibility was given by the plastic substrate. In 1968, Brody and his team managed to assembly the first flexible thin film transistor (TFT).[35] After 1997, when poly-Si TFTs on plastic were reported,[36][37] the flexible electronics became an hot topic and the research started to expand rapidly. Actually flexible electronic can lead to surgical and diagnostic implementation, naturally integrated with human body for an extremely innovative therapeutic perspective, or to wearable communication devices, or even, it can be the accelerator for the realization of the *internet-of-things*, thanks to energy self-standing sensors, and many other applications.

There are two approaches toward flexible electronics. The first profits by the elementary mechanic result according to which the bending strain decreases linearly with

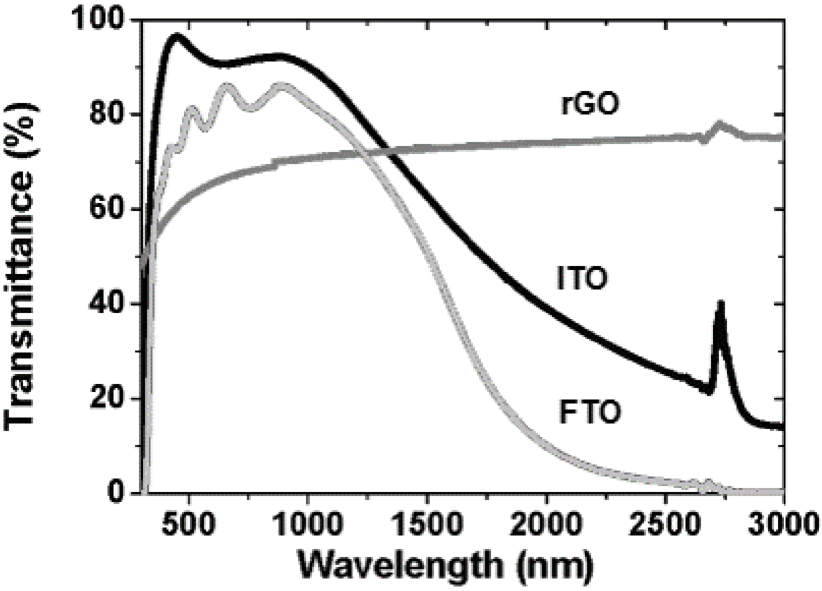

Figure 1.5: Transmittance spectra of ITO (black), 10nm thick film of thermally reduced GO (dark grey), and FTO (light grey) as function of incident wavelength.[29]

thickness: this means that any material can be flexible, if you can make it thin enough. If a Si wafer is rigid and brittle, wires, nanoscale ribbons, or membranes of silicon are not and building up systems on elastomeric substrates where these flexible structures are shaped in a wavy form guarantees not only flexibility, but also stretchability and compressibility. (See Figure 1.6). The second approach relies on new materials, such as elastic conductors, that can be the constituents of flexible electrodes, active components of flexible devices or that can play the role of electrical interconnections between bendable or even rigid devices.[38] Among these new materials, a key role is played by graphene, for its unique electrical, mechanical and optical properties. The graphene properties can be complemented and enhanced by 2D crystals such as boron nitride (BN) and transition metal dichalcogenides (TMDs), just to cite the most promising two.[39]

For what concerns the fabrication techniques of the structures, the flexible electronic field can take advantage from the standard production methods. Indeed, in the transfer-and-bond approach is used a carrier substrate, like a glass plate or a Si wafer, on which the structure is fabricated and then transferred from there to a flexible substrate. Since the tools for microfabrication have been developed to work in plane, the transfer has to be done as late as possible in the process. The drawback of this approach is the limited surface coverage, together with the costs. A second approach, which yet cannot benefit of the standard fabrication technologies, consists in in loco fabrication of the electronics, directly on the flexible substrates. Apart from developing new process techniques and using new materials, direct fabrication requires relying on amorphous or polycrystalline semiconductors, which are suitable to be grown on foreign substrates, such as polymeric ones, that in turn cannot tolerate high temperatures; for this reason, in direct fabrication, it is imperative to strike a compromise between low-temperatures processes and device performances.[40]

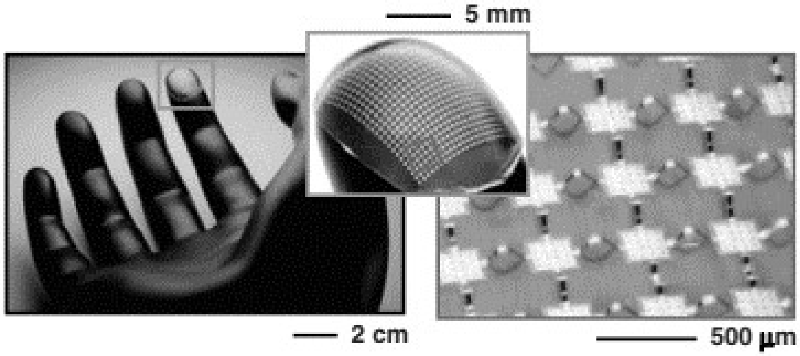

Figure 1.6: Stretchable silicon circuit with a mesh design, wrapped onto a model of a fingertip.[38]

Chapter 2

Materials, methods and instruments

2.1 Graphene Oxide

The GO used for all the experiments is purchased from Graphenea. This is not a cost-oriented choice, since pure graphite has lower costs and the Hummer method itself is quite inexpensive. We want yet an evaluation of the reduction procedure without any further trouble derivable from the graphene oxide production, which has been already extensively studied.[8 15 41] We purchase GO by Graphenea in water dispersion with a concentration of 4mg/ml, which undergoes stringent quality controls to ensure high quality and good reproducibility. In Table 2.1 we report the information on the GO properties given by the producer.

SEM and TEM images are furnished too, as well as elemental analysis through XPS (see Figure 2.1), where the analyzed sample consists in 2g of 4wt% GO in water, dried under vacuum at 60°C overnight. The data of the elemental analysis are reported in Table 2.2.

Form	Dispersion of graphene oxide sheets
Sheet dimension	Variable
Color	Yellow-brown
Odor	Odorless
Dispersibility	Polar solvents
Solvents	Water
Concentration	4 mg/mL
Monolayer content (measured in 0.5mg/mL)	>95%*

Table 2.1: Properties of Graphenea Graphene Oxide as given by the supplier.[42]
(*) 4mg/ml concentration tends to agglomerate the GO flakes and dilution followed by slight sonication is required in order to obtain a higher percentage of monolayer flakes.

Carbon	49-56%
Hydrogen	0-1%
Nitrogen	0-1%
Sulfur	0-2%
Oxygen	41-50%

Table 2.2: Elemental analysis of a Graphenea GO sample of 2g 4wt% dried. Correspondent XPS graph reported in Figure 2.1.[42]

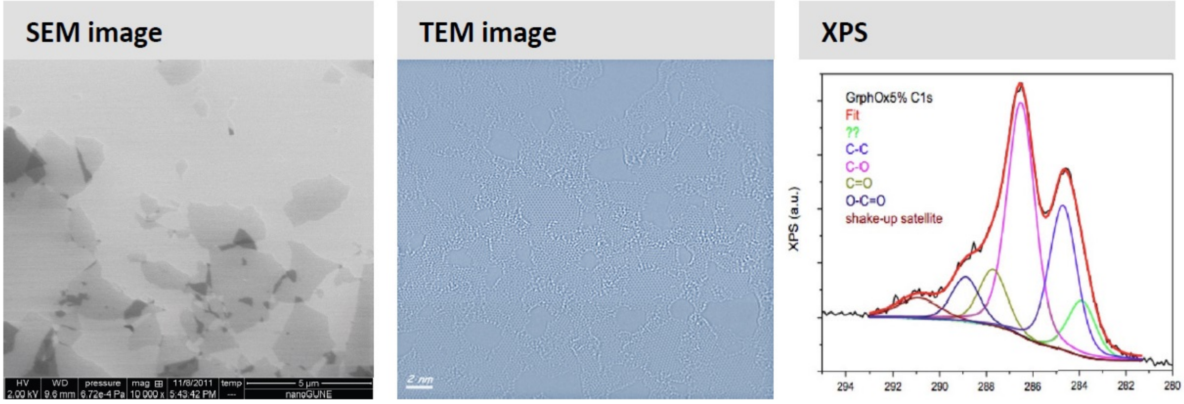

Figure 2.1: SEM, TEM and XPS data of 2g 4wt% dried GO of Graphenea.[42]

The product is stable at room temperature and we keep it in the original bottle, sealed with Parafilm M to avoid unwanted change in concentration, or in vials with lower capacity for easiness of usage. We pay particular attention, every time we open the bottle, to be far from any heat or humidity source, not to modify the dispersion concentration by water condensation or evaporation.

2.2 Rhodamine 6G

Rhodamine 6G (or Rhodamine 590) is a dye, whose molecular structure is shown in Figure 2.2. It is by far the most used dye for fluorescence tracing and lasing medium.[43] It is safe to use (it is harmful only if swallowed) and commercially available. We use Rhodamine 6G purchased by Sigma Aldrich with Dye content ~95%. In addition to its previously mentioned uses, Rhodamine 6G is a good dopant for graphene. Indeed, R6G on graphene has the tendency to constitute a network of dimers (two molecules $\pi - \pi$ stacked along the xanthene backbones), from which arises an extended π-electron system. Thanks to this, R6G can form $\pi - \pi$ stacking with graphene, which is essential for the doping that the R6G exert on the rGO.[44] Because of its structure with both electron withdrawing and donating groups, R6G could potentially dope graphene both positively and negatively, but experimental results show that in facts there is electron donation by Rhodamine.[44]

As mentioned, R6G is a red dye, with a peak of fluorescence at 556 nm and a range of absorbance between 440 nm and 570 nm, with a maximum at 530 nm.[43] These values are referred to ethanol solution, since they vary according to the solvent.[45] It is interesting to note that graphene oxide quenches the fluorescence of Rhodamine.[46][47] Since there is almost no overlap between the graphene absorption spectrum and the steady-state fluorescence spectrum of R6G, the quenching is assumed to happen through electron transfer,[48] instead of resonant energy transfer. The direction of this transfer is from Rhodamine molecules to graphene oxide.[46]

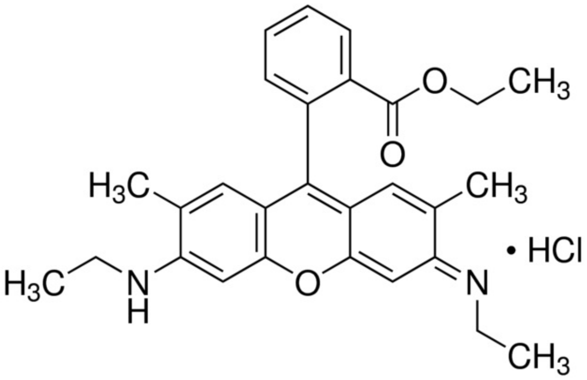

Figure 2.2: Rhodamine 6G molecular structure.

2.3 Deposition technique

The graphene oxide film are prepared by spin coating of a GO water/ethanol dispersion on quartz or silicon/silicon oxide substrates. According to our goal of having transparent, conductive films, what we need to measure are transmittance and sheet resistance; therefore, a quartz substrate is necessary. The films deposited on Si/SiO_2 substrates are instead the starting point to make three-terminal devices, useful to characterize the electrical properties of the films under a gate voltage applied through the p-doped silicon.

To obtain a uniform film of the desired thickness, we perform two-fold spin-coating. This is possible thanks to the insolubility of the dry GO film in the water/ethanol mixture used. Therefore, if a higher thickness is desired, it is sufficient to repeat the procedure until the wanted thickness is reached.

The solution we use is graphene oxide 1mg/ml in water/ethanol 1:3 mixture. Before use, the solution must be shaken (and not stirred: it causes flakes aggregation) to avoid the production of non-uniform films. The non-uniformity can be represented by sputters and/or by the presence of darker lines radially displaced. This is due to the partial precipitation of GO flakes in the solvent, because of the difficult solubility of GO in ethanol. We obtain films with the same defects even if we wait a long time between dropping the solution on the substrate and effectively starting the spinning. Time, speed and acceleration of the spinning, as well as cleanliness of the substrate, can influence the uniformity of the film, too.

Therefore, we keep on using a well-defined recipe, where only the quantity of solution varies according to the different sizes of the two substrate, and their specific wettability. For the Si/SiO$_2$ substrates, we drop 120 μl of solution for each spinning, and for the quartz substrate, we use 450 μl and 250 μl of solution for the first and second spinning respectively. Each spin coating process lasts 150 seconds, with 3000 rpm speed and 1500 rpm/s acceleration.

We choose the spin-coating technique because it leads to more uniform films in comparison with other techniques, such as drop-casting or solvent-induced precipitation,[19] and it is well repeatable. Dip coating[20] and vacuum filtration[28] are other possible methods for GO films deposition from suspension.

To tune the thickness of our films, we prefer to perform multiple spinning instead of varying the concentration of our solution. Indeed, it has been observed that at increasing concentration, there is also an increase of the degree of disorder.[19] The disorder is avoided depositing one layer on top of the other, probably because in a low-concentrated dispersion the flakes have enough space to rearrange their position, minimizing folding and superposition. It is important to underline that this is possible thanks to the ethanol dilution of the pristine water dispersion: since GO is poorly soluble in ethanol, the solution dropped on top of a dried film does not damage the underlying film.

2.4 Annealing process

A successful result in the production of a good rGO film depends largely from the annealing procedure. It is characterized by many crucial parameters, such as temperature, heating time, annealing atmosphere and heating ramp, which can be constant through the whole process or it can vary in proximity of critical temperatures. The choice of these parameters is sometimes limited by the set-up, especially the annealing atmosphere and the maximum temperature.

We perform the annealing on the heating stage of a Plassys evaporator ME400B placed inside a glovebox, as an assurance of the control of the annealing atmosphere. We take always care of starting every annealing in high vacuum ($\sim10^{-8}$ torr), but in case of lack of the vacuum system, the incoming atmosphere would be nitrogen, without damage for the sample. Generally speaking, high vacuum is preferable for a good reduction procedure, since it guarantees a residual-free sample and it avoids interaction between the film and the ambient residual oxygen.

For what concerns the reducing temperature, we analyze a wide range of temperatures, in particular 150°C, 250°C, 450°C, 550°C, 700°C and 1000°C. Choosing these values, we want not only to improve the good results in terms of conductivity already obtained ad high temperatures,[19 29] but also to investigate the low temperature region, playing with the reduction time and looking for acceptable results at more affordable conditions.[49] For each temperature, we test the film performances after two, five and eight hours of annealing. 1000°C is a particular case, since our set-up cannot stand such a high temperature for more than 40 minutes (one hour, if the heating is very fast).

The heating ramp is, instead, the speed at which the sample temperature reaches the final one, expressed in °C/min, and we heat the first set of samples with a constant rate of 5°C/min. In the initial project, the use of this heating ramp was a preliminary approach to select the best temperatures and timing over the whole range. The heating ramp of 5°C/min is acceptable because it prevents a complete film exfoliation as a consequence of the pressure of the evolved gases during reduction,[19] but it could be more gentle (1°C/min), possibly leading to better performances, even if it would be more time demanding.[68] During the experiments, in fact, we analyze the mass loss the sample undergoes before reaching the annealing temperature. We find out that, instead of slowing down the whole process, it is more efficient a multiramp approach. This consists in a very gentle heating of 1°C/min applied for a finite range of temperatures around a critical reduction point, when the film is most probably exfoliating;[68] out of this range, it is safe to perform a faster heating ramp to reduce the time demand of the process and without considerable film loss. For this reason, a second set of sample undergoes a heating process where up to 150°C the heating is of 20°C/min, up to 200°C is of 1°C/min and after is 50°C/min. Potentially, out of the 150-200°C slow range, the heating could be instantaneous. We choose these ramps of 20°C/min and 50°C/min so that the system effectively has enough time to slow down at 150°C and change the heating rate and the final temperature can be reached exactly. The details of the selection of the slow-heating range are discussed later in the Section 3.5.

After the annealing, we let the sample cool down to room temperature inside the bell of the evaporator under high vacuum. The high time demand of this way of cooling is justified by the fact that it prevents any impurity from contaminating or reacting with the hot sample. We keep the sample in air only the time necessary to the measurements, to avoid humidity absorption, which, as shown in Section 3.7, leads to degradation of the performances, probably because it induces an increase of the spacing between the rGO layers. For this reason, the sample are stored under controlled atmosphere.

2.5 Device fabrication

To better analyze the electrical properties of thermally reduced graphene oxide, we build bottom-gate top-contact field-effect transistors, to provide a gate voltage to the film. (See Figure 2.3)

The intention is to evaluate the drain current as a function of the applied gate bias, expecting to see an ambipolar behavior in rGO as it happens in graphene.[3] For this reason, we spin coat the graphene oxide on a silicon substrate with (230±10) nm thick thermal SiO_2 on top. The deposition recipe is the same as for quartz substrates, apart from the quantity of solution deposited, which is lower with respect to the one used for quartz, because the silicon substrate is smaller.

Before the annealing, we take care to clean the edges of the sample with ethanol and physically scratching the film to remove any possible percolation path between the rGO and the Si substrate. The presence of some connection between silicon and rGO film would cause leakage current. It is fundamental to do this before the reduction; otherwise, the annealed film would be too hard for a complete removal. Starting from this hint, we investigate further the issue of the mechanical properties of rGO, and the result are presented in Section 3.9.

When placing the sample on the annealing stage, where it is hold still with metallic clips, we take care to fix them on the edges of the sample, not to scratch the center of the film. We anneal the samples on Si/SiO_2 at a maximal temperature of 700°C, because silicon and silicon oxide have quite different thermal expansion coefficient and we do not want to induce lattice mismatches because of the too high temperature, since these could lead to undesired leakage current.

After the reduction, we evaporate interdigitated electrodes of 40 nm thick gold. On each sample, there are four pairs of electrodes with channel length of 60μm, 80μm, 100μm and 120μm.

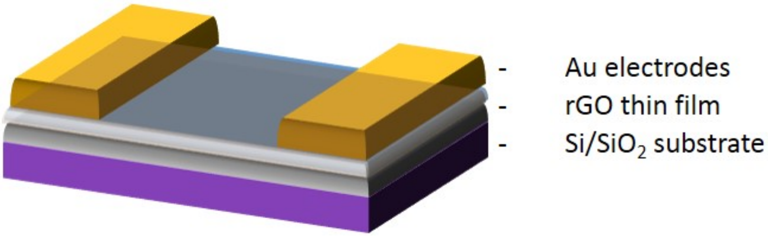

Figure 2.3: Schematic representation of the three terminal device made to investigate the electric properties of the rGO film.

2.6 Film transfer

The method of thermal reduction of graphene oxide requires high temperatures, which are not compatible with flexible substrates. To meet the goal of flexible and transparent electrodes made of thermally reduced GO, we need to reduce the film on a proper substrate first, and only after the reduction, transfer the rGO film on a flexible substrate.

The transfer of the film presents two technical issues: detaching the film from the original substrate without breaking it and obtaining a transferred film free from impurities deriving from the chemicals used or from the previous substrate. The goal is to have unchanged film properties before and after the transfer.

We start from films deposited on Si/SiO_2 substrates. The procedure we follow consists first in securing the rGO film under a spin coated PMMA layer, to protect the film from scratches and to minimize breaking or folding during the transfer. To detach the film from its original substrate, we proceed etching the silicon oxide: the whole sample is immerged in a 30% KOH water solution at 60°C. The heat helps the etching reaction and in few minutes the detachment is complete: the substrate lies on the bottom of the well while the rGO film with PMMA coating is floating (See Figure 2.4, left). The film must be washed from residual KOH that would otherwise crystalize, so we fish it with a clean bare silicon substrate and immerge it again in clean water (See Figure 2.4, center). This procedure is repeated three or four times for each film. The PMMA overlayer keep the film safe from breaking under these solicitations. The last fishing is made with a clean and dust-free PET substrate from the top (See Figure 2.4, right). In this way, the PMMA is placed between the film and the substrate and it is not necessary to remove it for the following electrical measurements. To remove residual water drops trapped under the film, we use a nitrogen gun to drive them away, and then we let the sample dry at 80°C.

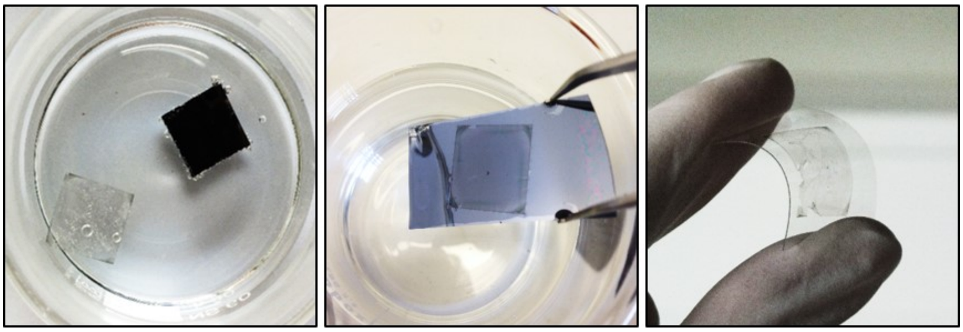

Figure 2.4: Principal steps of the transfer process. *Left* rGO film with PMMA coating detached from its pristine Si/SiO_2 substrate, both immersed in warm 30% KOH water etching solution. *Center* rGO film fishing with clean silicon substrate and washing in clean water. *Right* rGO film transferred on a PET substrate.

We use the same transfer method also to have suitable samples for the mechanical characterization of the film by AFM Force Spectroscopy technique described in Section 2.7.3, whose results are presented in Section 3.9. In this case, the substrate we need is still a Si/SiO$_2$ one, but patterned with micrometric stripes and squared wells of 5μm, 3μm and 1μm side. Actually, the wells of 1μm, because of the production method, are almost circular. The presence of the wells makes this substrate not suitable for a direct deposition of the GO solution. The wells are yet necessary for the measurements of the force-displacement curves, from which we can calculate the Young modulus of the rGO film, as it is explained later in this work. For the kind of experiment we want to perform, we need to remove completely the PMMA layer, so in this case we have to do the last fishing with the patterned substrate from the bottom, as to have the final configuration with the rGO film sandwiched between the substrate and the PMMA layer on top. Then, we dry the sample with nitrogen flow, careful not to break the film suspended over the wells, and we let it dry for two hours at 50°C. Finally, we remove the PMMA by warm acetone washing, which is safe for film and substrate and it is residual-free.

2.7 Atomic Force Microscopy

As a part of the big family of the scanning probe microscopy techniques, the Atomic Force Microscopy (AFM) is of particular interest for the surface analysis: it is able to probe the morphology and the molecular forces with sub-nano spatial precision and high force sensitivity.[50][51] Moreover, it can work in a wide range of conditions, from vacuum at cryogenic temperatures to ambient conditions of pressure and temperature, monitoring from individual atoms hopping[52] to biological reaction while they are occurring.[53] Its enormous potential resides in the scanning tip, nanometer-sharp and with many possible features (conductive, very hard, ultra-sharp and/or highly reflective, just to mention some options).

The Atomic Force Microscope feels the sample's surface physically thanks to the tip located at the end of a very sensitive cantilever, and the output is a height map. The cantilever is in fact free to deflect according to the forces that act on the tip when it is close to the surface. There is a force transducer, which is in charge to optically detect the cantilever deflection by a laser beam. The laser beam points indeed on the back side of the cantilever and from there it is reflected on a position-sensitive detector (PSD). The PSD is a photodiode composed of four quadrant that is able to convert the horizontal and vertical deflections into voltage signal. A feedback system takes advantage of this signal to keep the tip at a constant distance from the surface (in case of contact operation mode) or make it oscillate with constant amplitude (for tapping operation mode). This means that the interaction force between tip and sample is kept at a fixed value, making the atomic force microscope much more sensitive than its precursor, the stylus profiler, where the probe touches the surface in an uncontrolled way. The feedback control type employed in AFMs is a Proportional-Integral-Derivative (PID) one.

The movements of the tip on the sample surface and in the z direction are achieved by piezoelectric stages. Generally, they are synthetic ceramic materials that undergo geometrical changes when an electric potential is applied. The typical expansion coefficient of a single piezoelectric device is 0.1nm per applied volt.[54] With the aim of maintaining a set distance between sample and tip, the z piezoelectric moves up and down and the amount of vertical shift is assumed to represent the sample topography. The piezoelectric elements controlling the x-y movements are used to scan in a raster-like pattern the probe across the surface. This design, where the tip moves on the sample, is called probe-scanning configuration, and it is the opposite of the sample-scanning configuration, where the suspended tip is held fixed and the sample moves underneath it. The probe scanning-configuration has the advantage of being sample-mass independent. Almost every size of sample can be scanned and many accessories as liquid cell or optical options can be integrated. However, the construction is much more difficult: an entire tip plus optical-lever assembly is moving and the constructor must pay much attention not to introduce further vibrations into the probe.

In addition to the constructive features described by now, what really makes the AFM such a versatile and powerful tool is the possibility of choosing via software different scanning modes, opening up the atomic force microscopy to a wide range of possible samples, experiments and collectable data. The principal modes we are going to illustrate here are two topographic modes of large use: the contact mode and the tapping (or intermittent contact) mode. We will also briefly discuss the force spectroscopy, a non-topographic mode that we are going to take advantage of for the investigation of some mechanical properties of the rGO film.

2.7.1 Contact mode AFM

The most common AFM mode and the first to be developed is the Contact Mode, which, as the name says, works in the repulsive forces regime (see Figure 2.5) with the tip constantly in contact with the surface during the raster scan. The vertical deflection of the cantilever is kept at a constant set point thanks to the feedback loop acting on the Z piezo. In this way, a constant distance between surface and tip is maintained during the scan and topographic data can be collected according to the position of the Z piezo.

The constant touching between tip and sample has obviously some implications: during the scanning, both the sample and the tip can be damaged or changed by the process, and the final topographical result can be affected by the nature of the surface or by the lateral forces that the tip experiences being so close to the sample. Anyway, the limitations of the contact mode acted as promoters for the development of other methods and despite everything, this technique is still very powerful: it is the fastest topographic one, since the cantilever deflection is directly related to the topography of the sample, it guarantees high-resolution images and it is strongly recommended for imaging in liquid.

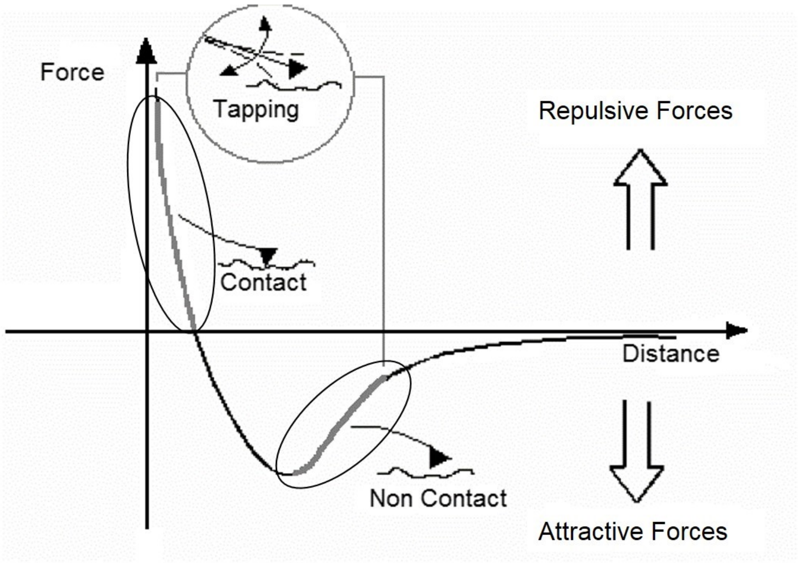

Figure 2.5: Lennard-Jones potential showing the kind of forces (attractive and repulsive) acting between sample surface and tip, according to the distance between the two. AFM modes differs mostly for the regime of forces they work in: *contact mode* works in the repulsive regime, *non-contact* in the attractive one, while in the *tapping mode*, where the tip is oscillating, the instantaneous tip-sample distance varies so much to cover almost the whole range of forces.[55]

2.7.2 Tapping mode AFM

The tapping mode is the main AFM oscillating mode. It has been principally developed to take advantage of the benefits of a modulated signal, such as the high signal-to-noise ratio that allows measurements with very small tip-surface forces involved. The working principle consists in making the cantilever vibrate near its resonance frequency by an oscillating input signal given to an additional piezo attached to the probe holder (see Figure 2.6). The system monitors the oscillating amplitude, which is modified by the feedback system as to keep it constant, according to the tip interaction with the sample. The PSD detects the amplitude changes, which can be related to the effective distance between the average tip position and the surface. The feedback to the Z piezo, the one used to keep the amplitude constant, is what generates the topography of the sample.

The tapping mode scanning can also give additional information. One example is the phase contrast, a qualitative property originating from the different mechanical responses (i.e. elasticity) of a many-component sample: the phase shift between input and output signals due to the tip-sample interactions varies according to the material and can be recorded and plotted on a color map to individuate the composition of different areas of the sample. In comparison with the contact mode, the tip-sample contact time is

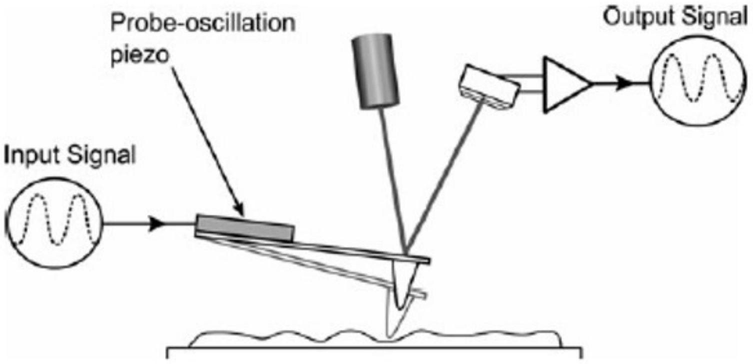

Figure 2.6: Schematic setup of the tapping mode, where an oscillating input signal makes the cantilever vibrate at a frequency close to its resonance one. The interaction forces between tip and sample determine the actual oscillation, monitored via PSD. The oscillating output signal is compared with the input one to determine the forces acting on the tip and therefore the sample topography.[54]

much shorter and the involved forces weaker, resulting in a minimized sample damage. Because of the perpendicular movement of the tip with respect to the sample, the lateral forces are almost eliminated. However spurious resonances can be caused by a liquid working environment and this kind of imaging can be tricky.[56]

2.7.3 Force spectroscopy

Force spectroscopy is a non-topographic mode of the AFM. Non-topographic means that the information we collect are other than topography. In this case, we can obtain information on the forces acting between the sample surface and the contacting molecules on the end of the tip. This mode does not involve an x-y scanning: a position is manually selected and there the probe performs a ramp in the z direction, during which the software measures the deflection of the cantilever while approaching and retracting from the sample surface (see Figure 2.7). It is important to underline that the speed of approach and withdrawal of the tip from the surface affects the measurements. From the simple recording of force-distance curves, we can study the nanoindentation, the elasticity of the sample and its interactions with the probe. From the adhesion data indicated in Figure 2.7 we obtain the information for the proper force spectroscopy, as these data are symptomatic of the interaction between probe and surface. From the slope data, we can get two kinds of information: if the sample lies on a flat, continuous substrate, then we can study the nanoindentation process; instead, if the sample is a film suspended on a hole, we can derivate its elastic modulus. Of course, it is necessary to know all the properties of the tip: hardness, material and coating of the probe for nanoindentation

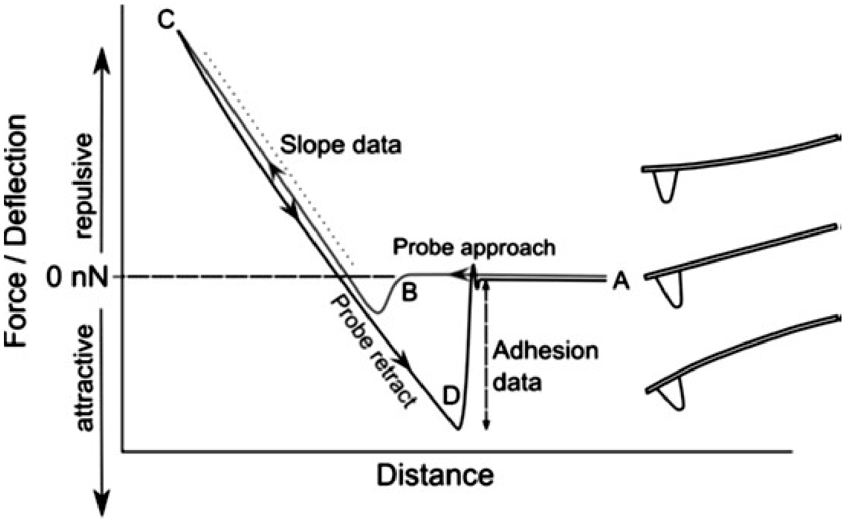

Figure 2.7: Ideal force-distance curve. At A the probe begins to approach the sample surface but it is still far from it. At B, attractive forces start to pull the probe to the surface, but they soon become repulsive as the probe keeps on moving toward the sample. C is the inversion-of-motion point and it is user-defined. When the force applied to the retracting cantilever overcomes the tip-sample interaction, a pull-off occurs.[54]

and force spectroscopy, and stiffness of the cantilever for elasticity measurements. The tip is in fact our reference and has to be chosen carefully.

We are interested in the Force Spectroscopy technique because it is useful to investigate the mechanical properties of the rGO film. In particular we take advantage of this method to measure the elastic modulus of suspended rGO membranes (see Section 2.6 for the device fabrication, Section 3.9 for the measurement and analysis process).

2.7.4 AFM tips

The AFM tips are an essential element of the instrument and are composed of a cantilever and a probe. Usually the materials used for the cantilevers are silicon nitride (Si_3N_4) and silicon (Si). According to the operating mode, there are different requirements for the tip. For example, the cantilevers for contact mode tips are fabricated from either silicon or silicon nitride, but they must have a very low force constant, typically smaller than 1N/m. This is because a very stiff cantilever is probably going to damage both the sample and the tip in the contact mode. On the other hand, cantilevers for oscillating modes are stiffer, not to vibrate with enormous amplitude and in an uncontrolled way when solicited, so they are usually made of silicon and have force constants greater than 10 N/m.[54] The differences between tips for contact- and tapping-mode go on concerning the form of the cantilever: usually v-shaped for the first, rectangular for the second. Moreover, the probes can differentiate for shape, sharpness, aspect ratio, coating (conductive, magnetic, highly reflective), that are all going to affect the results and should be carefully selected.

For the special use we make of the AFM when measuring the elastic properties of the film (see Section 3.9), we must pay much attention in the choice of the tip. The requirements are: high cantilever force constant, to avoid the situation where the probe press against the membrane and the cantilever deflects before the membrane; tip not too sharp to avoid nanoindentation before deflection; hard tip to prevent its breaking or modification that will affect the data. Following these criteria, we use a Non-Contact/Soft Tapping Silicon Tip with elastic constant of 41 N/m and 7 nm probe radius. We calibrate the cantilever elastic constant personally, as to include the elastic effects of air and water film on the sample. To do this, we record a force curve on a clean quartz substrate that is assumed perfectly rigid, so that what we measure are the properties of the system air-water-tip only.

2.8 X-rays Photoelectron Spectroscopy

X-Ray Photoelectron Spectroscopy (XPS), also named Electron Spectroscopy for Chemical Analysis (ESCA), is a largely used spectroscopic technique based on electron emission for the analysis of the surface chemistry of a material. In particular, measuring the number of electrons emitted from the first 10 nm of the material and recording their kinetic energies, the XPS is able to identify and quantify the presence of all elements from Li to U existing in the surface at >0.05 atomic %, revealing also the chemical environment where the elements exist in. H and He are not detectable because XPS is designed for core electrons analysis and these elements have an extremely low photoelectron cross section.

The collected electrons are emitted from surface atoms after the collision with an incoming photon. During the photon-electron interaction a complete energy transfer occurs, that sets the electron free from the core of the atom. This is possible only under one condition: the energy of the incoming photon must be enough to overcome the energy binding the electron to the atom. For this reason, highly energetic photons, such as X-ray ones, are necessary. The measured quantity is the electron kinetic energy (E_K), a discrete value that is a function of the incoming photon energy, which is known, and of the electron binding energy (E_B), which is element- and environment-specific. The final spectrum is built using the derived E_B^{XPS}, instead of the recorded E_K^{XPS}, because the binding energy is independent from the X-rays one. The superscript XPS is used to denote the fact the value we measure does not correspond exactly to the one expected for a ground-state atom: the actual E_B values are in fact altered by the core hole created with the photoemission. This is called final state effect, but the variation from the expected values is very small. The relationship between the involved quantities was

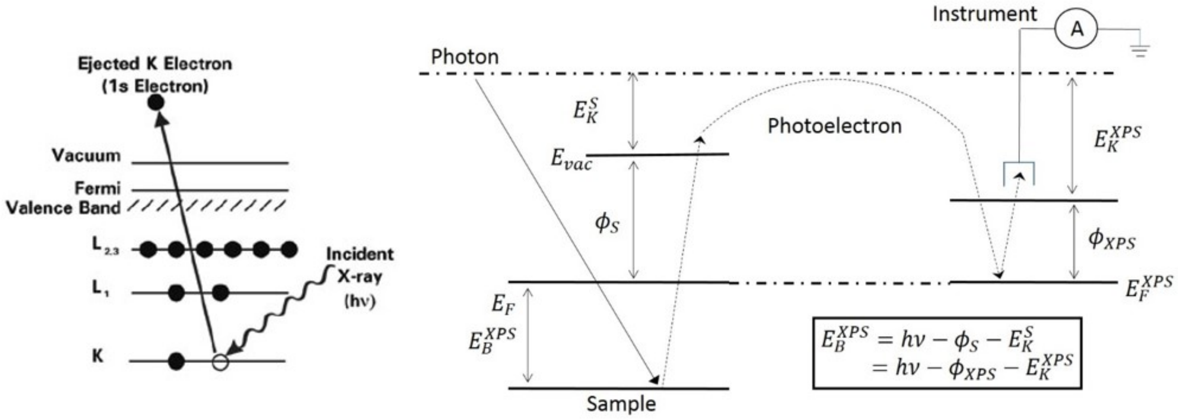

Figure 2.8: *Left* Schematic example of the photoelectron process with the various electronic energy level labelled with the X-ray notation. *Right* Relation between work function, Fermi energy and kinetic energy of/from the sample and the instrument.

developed by Einstein in 1905 and it is the following:

$$E_K^{XPS} = E_{ph} - \phi_{XPS} - E_B^{XPS}$$

where ϕ_{XPS} is the work function of the instrument. The work function of the instrument is used to avoid any dependence of E_K^{XPS} from the work function ϕ_S of the sample. Actually, the instruments are designed so that the ϕ_{XPS} value is smaller than the one of almost any sample: since in the sample-instrument contact the Fermi levels align, the dependence on ϕ_S is replaced by dependence on ϕ_{XPS}, as illustrated in Figure 2.8, right. The influence of ϕ_S persists only in defining the cutoff energy: if the electrons cannot overcome their ϕ_S, they cannot be detected. De-excitation processes are likely to follow the photoelectron emission and among these the two primary are the Auger process and the termed fluorescence: the first results in an electron emission too, and it is therefore observed in the XPS spectra; the second consists in photon emission.

Usually the analysis is carried out by focusing on particular photoelectron signals only after a recollection of the spectra over all accessible energies. This ensures an accounting for all the elements during quantification.

The XPS setup primarily consists of an X-ray source, an extraction optic with an energy analyzer, and a detection system for the extracted electrons.

The X-ray sources are most commonly X-ray tubes (that are divided in monochromated sources and standard sources) and, where the facilities allow it, Synchrotron sources. We will focus on X-ray tubes, that produce X-rays by directing an energetic electron beam at a metallic solid called X-ray anode, the cathode being often a thermionic source. Aluminum is the most commonly used anode, because Al- Kα radiation has relatively high energy and intensity, combined with minimal energy spread, together with

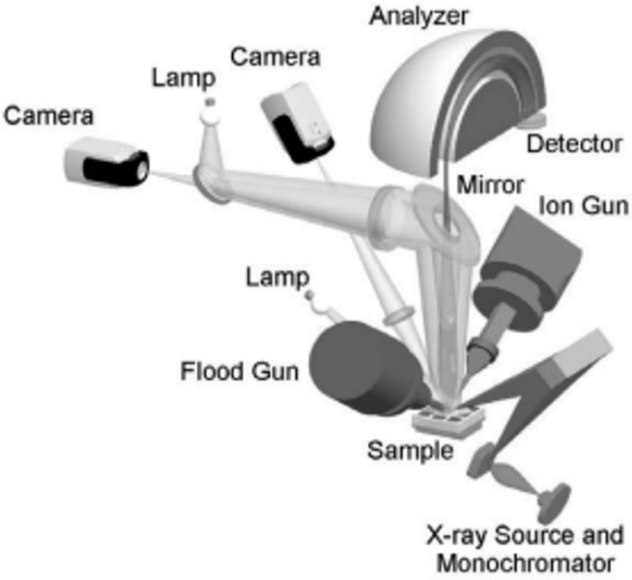

Figure 2.9: XPS components.[57]

the fact that Al is an effective heat conductor (important to have a long anode lifetime) of easy manufacture and use as anode. The Al-Kα X-rays (also called K$\alpha_{1,2}$ X-rays) comprise the Kα_1 and the Kα_2 peaks, that are separated by such a small amount of energy to be usually described together. They arise from the process involving a 2p level electron filling the 1s hole created by an incoming electron: the 1s-2p energy difference is then removed via fluorescence, that generates the Kα X-rays emission, or via Auger electrons.

The energy analyzer is the second key part of the XPS setup, being the filter that separates the electrons according to their energies. The most commonly used in modern XPS instruments is the Concentric Hemispherical Analyzer (CHA), constituted by two concentric biased hemispheres that deflect the electrons of some specific energy E_0 onto the detector. The operating mode can select a constant retard ratio (CRR) or a constant analyzer energy (CAE): the most commonly used is the last one, since accelerates/decelerates the electrons to some constant energy value E_0 before entering the analyzer. As long as the *pass energy* E_0 is held constant, the energy resolution is constant too, and it is improved in correspondence of lower pass energy values, but at the cost of less sensitivity. Resolution and sensitivity are both important to determine the quality of the data, since the XPS spectra are plotted in units of energy versus intensity. The detector must then be capable to measure not only the energy of the emitted electrons with good resolution, but also the number of electron produced, even recording individual electrons, and this depends upon sensitivity. It operates therefore in pulse counting mode, recording a signal in Ampere that is then translated in units of counts per second.

The basic setup explained here can be further implemented with an ion source, for surface controlled sputtering and consequent removal of surface layers for a progressive-depth analysis, and a flood gun, that aids charge compensation when analyzing insulating samples.[58]

Within the instrument, the electric and magnetic fields have to be minimized or, at least, accounted for, in order to not affect the E_K^{XPS}. Moreover, ultrahigh vacuum (UHV) is necessary to avoid the environment molecules to interfere with the measurement, for example scattering the outcoming electrons or absorbing the X-rays and being analyzed, too. An introduction chamber is used as an intermediate step for inserting the sample in the analysis chamber.

We perform XPS measurement to assess the evolution of the chemical composition of our film during the reduction, evaluating samples that are representative of the main steps of the process. The instrument we use for the reported measurement is a Thermo Scientific K-Alpha X-ray Photoelectron Spectrometer (XPS) using monochromatic Al-Kα radiation (hν=1486.6 eV).[57]

A first survey measurement is performed with a 200 eV analyzer pass energy and a 1 eV energy step size to calculate the atomic concentrations for each sample. Then, our particular interest being in the reduction of the sample by the progressive loss of bonds concerning carbon and oxygen, together with the restoring of C=C bonds, the C1s peak measurements are performed, the analyzer pass energy being of 50 eV and the energy step size of 0.1 eV.

Curve fittings of the C1s spectra are realized using a Gaussian-Lorentzian peak shape after performing a Shirley background correction, to finally obtain the relative percentage of each type of bond inside the analyzed sample. Since we are dealing with ultra-thin layered structures, the surface analysis that is performed by XPS can be confidentially related to the whole of the sample.

2.9 Electrical characterization

The electrical characterization of our rGO films follows two parallel pathway that depend from the sample structure. What we want to measure, in fact, are sheet resistance and gating effect. The sheet resistance measurements are performed on the films deposited on quartz because we want to correlate these data with the transmittance measurements, possible only on transparent substrates. The gating effect, instead, is an interesting property, that we measure in the samples on Si/SiO_2 substrates, where we apply a bottom-gate voltage. Therefore we will discuss them separately.

2.9.1 Sheet resistance

The sheet resistance R_S is an extensive property of 2D materials, comparable to the electric resistance. When an electric current flows through a thin film, the film opposes itself to the passage of the current, and the measurement of this resistance is called sheet resistance. The official unit is Ω, but the common one is $\Omega/\square$ or Ω/square. The sheet resistance is actually the volume resistivity times 1 mil, that is to say that of a thin film with an assumed thickness of 1 mil (=0.001 in =25.40 nm).[59] Such a thin film can be considered, with good approximation, two dimensional, and this is the reason why the sheet resistance is thought as a property of 2D materials. As long as the approximation holds (1mil thick films, or thinner), the sheet resistance can be accounted for; in thicker materials, we measure the volume resistivity.

The four point probe is the method to measure the sheet resistance. The probe itself is made of four thin tungsten wires collinearly placed which contact the sample surface at the same time and with the same pressure. Between the two external probes, a current flows, and a voltage is measured between the two inner probes, ideally without drawing any current.[60]

There are some requirements on the sample: the film thickness must be much smaller than the spacing distance between the probes, which are equally spaced; the sample must be semi-infinite, in practice the distance from any probe to the nearest boundary must be at least five times the probe spacing. If these requirements are fulfilled, no correction is needed.

Our four point probe head is a Jandel Cylindrical four point probe with wires of tungsten carbide with tip radius of 300μm and spacing between needles of 1mm. This spacing is big in comparison with the film thickness; therefore, we do not have to correct our results.

The four point probe head is placed in a Multiheight Probe stand with micrometer controlled X-Y stage (by Jandel), which allows to move the sample underneath the probe and to load the head on the film very precisely. It is advisable to place the head in the head holder and to regulate the height, testing it on a loose sample because the initial adjustment could damage the film. The head is connected to Jandel RM3000 Test Unit, which allows selecting the input current and gives as output the measured voltage or automatically the sheet resistance. We apply the minimum current of 10 nA and repeat the measurements in different position of the film, every time lifting the head first. This let us test the uniformity of the film and collect a statistic population. It is suggestible not to take measurements in proximity of the sample edges, not to lose the approximation of semi-infinite sample.

2.9.2 Gating effect

We test the current flowing through the film under the effect of a gate voltage in the samples deposited on Si/SiO$_2$ substrates. To do so, we use a probe station DPP210 by Cascade Microtech furnished with micromanipulators with gold tips, connected to a Keithley 2636A system.

The tips are carefully load on the top gold contacts, acting as source and drain. One of them is connected to the ground, the other is a voltage supplier and we read the drain current I_d flowing between them. The gate voltage is applied through the stage of the probe station, over which the sample is placed. While recording the I_d current, the gate voltage sweeps in the selected range with a set voltage step.

The whole setup is controlled by a LabView program, which also collects the output data and traces the resulting graphs. Thanks to it, we can also control the leakage (or gate) current, that has to be very small.

2.10 UV-vis-NIR transmittance measurements

The UV-vis-NIR spectrophotometry is the science that studies and characterizes qualitatively and quantitatively the photonic absorption and transmission spectra in the range of ultraviolet, visible and near infrared light. When a sample is irradiated with light, the radiation transmitted through it will differ from the incident one by a quantity corresponding to the absorbed light. Transmittance and absorbance are the two way to express the absorbed light and are respectively defined as:

$$T = \frac{I}{I_0} \quad (in\, percentage: \%T = \frac{I}{I_0} * 100) \quad A = -\log_{10} T = \log_{10} \frac{I_0}{I}$$

where I_0 is the intensity of the incident radiation and I the intensity of the transmitted one. Experimental observations relate through an exponential law the optical transmittance to the path length that the light has to travel inside the sample and to the concentration of the sample in case of a liquid one, to its density if it is solid.

The light-matter interaction that takes place during irradiation consists in the absorption of a photon of defined energy by a molecule, that it is promoted from its ground state to an excited one. This excitation is associated with an electronic transition from a low energy orbital to a high energy one, the difference between which corresponds to the energy of the absorbed photon. Since the separation between orbitals and their energetic orders are strictly characteristic of each molecular species, the absorption spectra are equally specific of each molecule. Molecular spectra are not sharp and separated lines as the atomic ones: they are instead large bands not well structured and this is because each single electron in its ground state can be promoted to many different vibrational and/or rotational levels, which are typical of the molecular structure (See Figure 2.10). The important feature of each band are its position and its intensity. The position is given by the wavelength, or the photon energy, of its maximum; the intensity, instead, depends on the absorption probability: the so called allowed transitions, the ones that are highly probable because they induce a consistent variation of the dipole moment, correspond to a high intensity in the absorption spectra, while the forbidden transitions present low absorption values. The $n \rightarrow \pi^*$ transition (from non bonding to antibonding of tipe π) for organic molecules, for example, is a forbidden one, therefore it is generally weak and hidden by more intense ones. The $\pi \rightarrow \pi^*$ transition (from bonding of tipe π to antibonding of tipe π), instead, is an allowed one, accordingly intense and typical of π conjugated systems and aromatic ones. These two transition are, however, the only two possible in the UV-vis range, because their energy requirements match with the wavelengths of the photons in this region of the light spectrum. It is also important to mention that at wavelengths lower than 200 nm the atmospheric oxygen absorbs very intensely and, apart from apparatus working in vacuum or inert atmosphere, this strong absorption covers all the others that hence cannot be investigated.

The spectrophotometer is the instrument that allows to measure transmittance and absorbance as a function of the wavelength of the incident radiation. It is essentially constituted by a light source that is combined with a monochromator for the selection of the light wavelength, then a sample holder and finally one or more detectors to measure the intensity of the transmitted radiation.

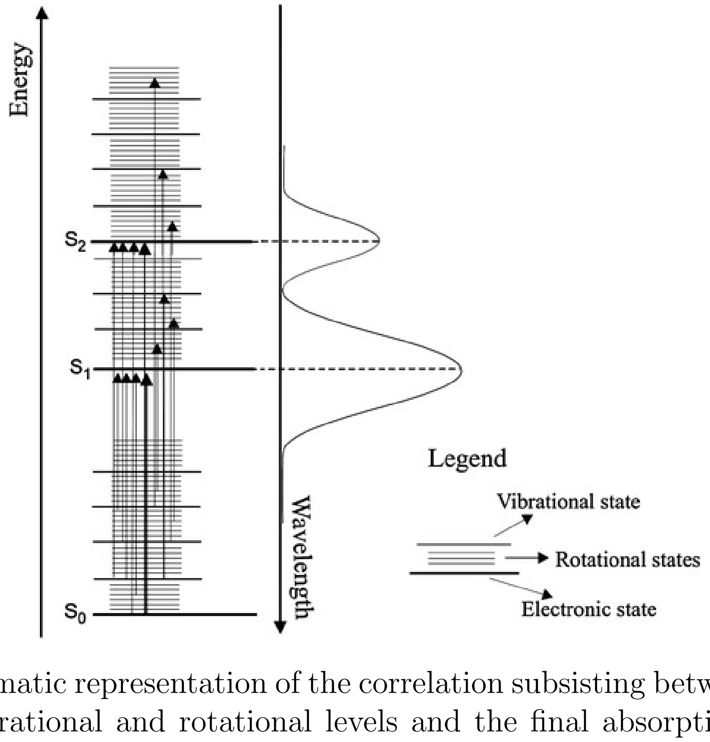

Figure 2.10: Schematic representation of the correlation subsisting between the electronic transitions to vibrational and rotational levels and the final absorption spectra of the molecules, explaining the presence of broad bands instead of sharp peaks.

The spectrophotometer is the instrument that allows to measure transmittance and absorbance as a function of the wavelength of the incident radiation. It is essentially constituted by a light source that is combined with a monochromator for the selection of the light wavelength, then a sample holder and finally one or more detectors to measure the intensity of the transmitted radiation.

The real apparatus is obviously more complex than this, and in particular involves many optical parts for the redirection and collimation of the light inside the instrument. The above mentioned elements have, however, a key role and deserve to be presented with some more details. First of all the light source: to cover the whole wavelength range, the light source is in fact composed of two different lamps, normally a deuterium one for the short wavelengths (180-350nm) and a halogen one for the longer wavelengths (330nm-NIR). The switch between the two lamps is done with a selector. Unfortunately, the combination of more sources, together with the type of sources itself, do not guarantee a constant intensity of the emitted light over the whole wavelength range. Therefore, it is advisable to record blank (no sample) and dark (obscured sample beam) spectra that will be subtracted from the final one, so that the influence of the lamp intensity on the measurements is minimized. The emitted radiation has to be processed by a monochromator to select the wavelength that will be redirected on the sample. There are two different type of commercially available spectrophotometer that mainly differ from now on: the monochromatic beam can be now directed on the sample, or split in two. The first option is characteristic of the single beam model, the second one of the double beam model. The splitting option has the meaning of having a constant reference of the incident light on a parallel path that can be subtracted from the radiation transmitted through the sample. In particular, this is useful for measuring a blank curve on all the elements of the sample that are not the molecule we are interested in, for example the substrate of a solid sample or the cuvette and the solvent of a liquid one. In the single beam model, this blank subtraction can be performed too, but the curves have to be recorded separately, losing the certainty that the incident light is the same for both measurements. In both cases, the transmitted light, properly corrected with the blank, reaches the detector that converts the light signal in an electric one. Modern spectrophotometer normally mount photodiode detectors or photomultiplier tubes.[61]

The spectrophotometer we use for the reported measurements is a double beam model named JASCO V-670 working in the UV-vis-NIR range (wavelength range 190-2700 nm), equipped with deuterium and halogen lamps, a thin-film sample holder and two photomultipliers tube for the detection.

2.11 UV-photoelectron spectroscopy

A photoelectron spectrometer is used to measure the work function of the here concerned rGO thin films. Based on photoelectric effect, the instrument, model AC2 of the Riken

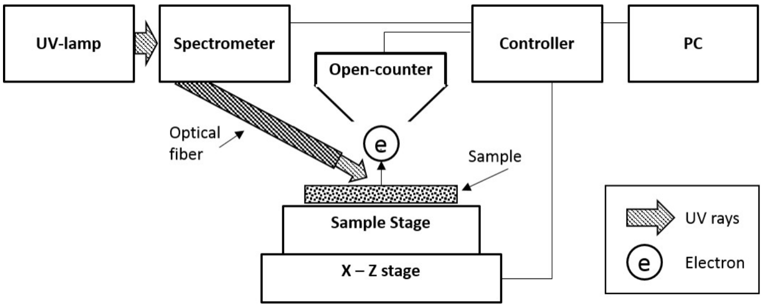

Figure 2.11: Schematic configuration of the UPS.

Keiki CO., LTD., is designed to measure the photoelectron emission of solid-state sample surface in air, at room temperature and ambient pressure.

The light source is a D_2 lamp, that is to say a low-pressure gas-discharge continuous UV-emitter. The light intensity is controlled by a light adjuster, before entering a spectrometer that selects the desired wavelength and redirects it to the sample through an optical fiber. A manual stage controller in the z-direction allows to adjust the vertical distance between the sample and the optical fiber, to have them as close as possible to each other. The UV-light spot on the sample has a size of $2{\sim}4$ mm^2 and the incident wavelength can be chosen between $346{\sim}200$ nm or, in terms of energy, the scan can be performed between 3.4eV and 6.2eV.[62] The irradiated sample, because of Einstein's photoelectric effect, emits photoelectrons from the surface (from several Å up to hundreds of Å of depth) that are detected by the open-counter. The open-counter is a photoelectron counter in an open detection chamber that is able to suppress the background noise produced by the photoelectrons originated from outside the subject by scattered rays.[63]

The resulting plot is the photoelectron yield as a function of the photoelectron energy over the set scanning range. At low energies, the plot is expected to be horizontal with a zero yield because the incident UV-rays do not have enough energy to extract photoelectrons from the sample. Once the work function energy value is reached, the curve shows a sudden increase of its slope: the incident photons excite the electrons in the sample that become energetic enough to be photoemitted ($h\nu \geq \varphi$, where φ is the work function of the sample) and the photoelectron yield increases hereafter with the energy. A linear relationship is obtained between the energy and the squared root of the yield for a metal-like sample and between the energy and the cubic root of the yield for a semiconductor-like sample. To calculate the exact value of the work function, the analysis program allows to select manually the Ground Level and the Regression Line: the work function is found as the intersection of the two. It is also opportune to perform a further data correction accordingly with the emitting power of the lamp at each energy value, known as the Quantity of Light coefficient. In this way, the electron count is no more a self-consistent value, but is coherently related to the intensity of the incident radiation.

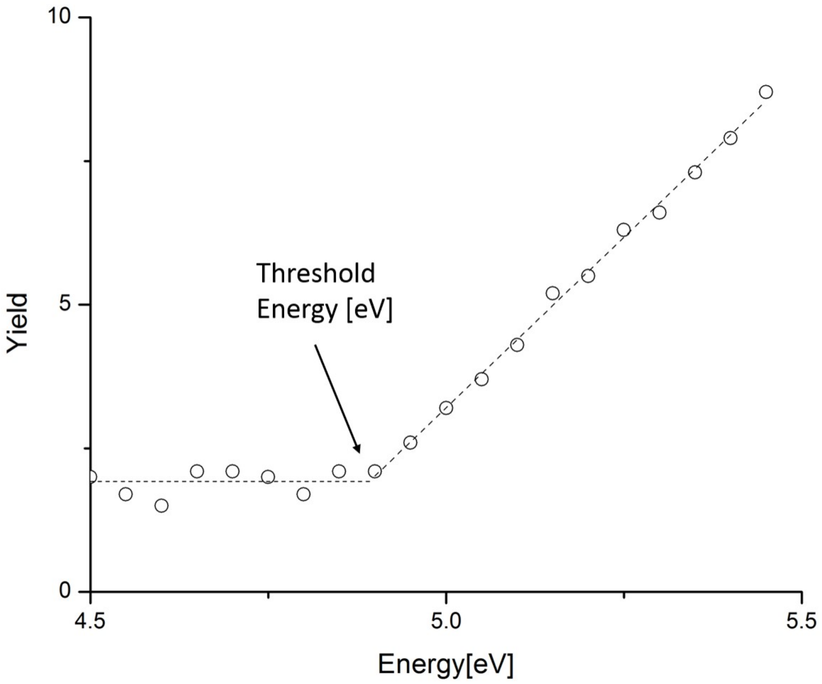

Figure 2.12: Exemplificative plot resulting from an UPS analysis. The yield is reported as a function of energy. The threshold energy is the interception of the horizontal baseline and the tilted regression line.

2.12 ThermoGravimetric Analysis

The TGA, acronym for ThermoGravimethric Analysis, is a technique that investigates the behavior of the mass of a sample as a function of temperature and time. Dynamic temperature curves or isothermal ones can be performed, during which the sample weight is monitored and finally its mass (or percent mass) is plotted against time or temperature. It is often useful to complementary evaluate the plot of the first derivative of the TGA curve, called DTG (Differential ThermoGravimetric), that is helpful to recognize the mass changes that are individuated by peaks, instead of steps as in the TGA curve. Many effects can cause a mass change and among them, drying and thermal reduction in an inert atmosphere (with gaseous products formation) will be of our particular interest.

The measurements we perform are achieved through a horizontal microbalance provided with a compensation system that holds the sample in the furnace in the same position even during mass changes. The balance itself is located in a specific chamber, purged with a protective gas, to avoid consequences due to the heat radiations effects and the possible income of corrosive decomposition products. The furnace opens sliding horizontally to allow the sample loading that in our case is performed by a precision robot. The furnace atmosphere can be chosen according to the specifics of the experi-

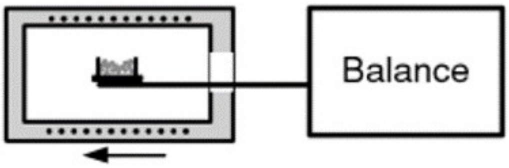

Figure 2.13: Horizontal arrangement of the thermobalance. The arrow shows the movement direction of the furnace for sample loading.

ment. The pressure inside the furnace is usually constant because the furnace is open to the external atmosphere at the outlet, but since the change in density of a heated gas can lead to artifacts in the data, buoyancy correction is needed. The correction can be done performing a blank experiment, using the same crucible that will be later filled with the sample and the same temperature program. The quantity of material placed in the crucible must respect the maximum capacity of measurement of the balance, but if the quantity of material is to small, there is the risk that the small mass changes and the final mass exceed negatively the balance resolution. Therefore, the sample mass must be carefully selected. The crucible choice is an important aspect: its material must not influence the reaction and it must stand high temperatures without problems. As it is generally done, we use alumina crucible, which can be heated to over 1600°C. The crucible must never be completely sealed, or it could explode, and must be in contact with the furnace atmosphere. This is done by removing the lid completely, placing it loosely on the crucible or sealing the crucible but piercing the lid. A completely open crucible allows faster reactions in the gas phase with respect to the other two configurations, in which the mass loss is shifted to higher temperatures. In addition, the heating rate can induce shifts of the peaks, too. These shifts are due to the thermal conductivity of the samples, which is different than that of the pure metals used to calibrate the temperature and adjust the instrument. In particular, the heating rate dependence is more evident in the region where the chemical reactions occur, and higher heating rates generally shift the reactions to higher temperatures. This can but be an advantage, in case we need to separate overlapping reactions.

Finally, the evaluation of the TGA curves involves the determination of step heights (sample mass change). To deal with unsure step limits and overlapping processes, DTG curves can be useful because mass loss steps appear as distinct peaks. Their integration can quantify the mass loss.

Another significant curve that can help TGA data evaluation is the Differential Scanning Calorimetry (DSC) curve, which is the record of the heat flow occurring in the sample while heated, cooled or held at constant temperature. Thanks to DSC curves, the reactions firstly individuated with the TGA can now be classified as endothermic or exothermic, the enthalpies of reaction and transition can be measured and the specific heat capacity can be determined. This is possible through the comparison of two pan temperatures: the sample one and the reference one. The heat flow is measured as the difference between the temperatures of the two pans divided by the thermal resistance of the sensor. If the system disposes of a double pan holder, the temperature difference between the sample and the reference pan can be measured directly by a thermocouple. In our case, where a single pan holder is present, the correct DSC curve can be obtained with reference to a previously measured blank curve that records the reference temperature, together with other parameters concerning the buoyancy correction for the TGA, as already mentioned.[64][65][66]

The instrument used for the following measurements is a TGA/DSC 2 produced by METTLER TOLEDO, schematically represented in Figure 2.14, which is furnished with a microbalance and presents a small furnace that can be heated up to 1100°C in 5 minutes. Temperature accuracy is of ±0.25 K and temperature precision of 0.15 K, weighting accuracy is of 0.005% and weighting precision of 0.0025%.

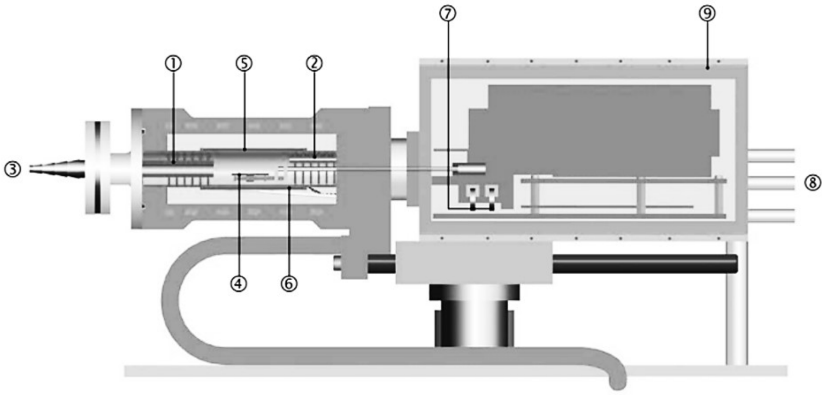

Figure 2.14: Explicative model of the TGA/DSC 2 by METTLER TOLEDO system used for the reported measurements. Principal elements: 1. Baffles; 2. Reactive gas capillary; 3. Gas outlet; 4. Temperature sensors; 5. Furnace heater; 6. Furnace temperature sensor; 7. Adjustment ring weights; 8. Protective and purge gas connector; 9. Thermostated balance chamber. Image courtesy of METTLER TOLEDO.

Chapter 3

Experimental

3.1 Film morphology through AFM characterization

In order to prove the uniformity of the film, and to measure its roughness and thickness, we perform AFM measurements both on pristine and reduced graphene oxide films.

The first approach is a check of the uniformity on large scale of the as-deposited film by optical microscope. As shown in Figure 3.1, the film does not show any discontinuity. There are few additional flakes deposited on the film, more visible with the dark field view, but they do not represent a defect and they should not compromise the quality of the film.

We proceed imaging the GO on quartz with AFM Dimension 3100 Bruker controlled by Nanoscope software. The images we obtain are important to evaluate more in detail the morphology of the film, to check the eventual presence of uncovered substrate areas, to calculate the film roughness as an indicator of a good deposition technique and finally to measure the thickness of the film.

Thickness measurements are possible with AFM, but we need to scratch the sample on purpose, possibly on a side not to interfere with the following electrical measurements (Figure 3.2). We take care to perform the scan with the probe moving perpendicularly to the direction of the scratch, and then we measure the height difference visible in Figure 3.2, right. This analysis, as well as images postproduction, are done with Nanoscope Analysis software released by Bruker, the producer of our AFM. We want to measure the thickness of our films because it can affect both conductivity and optical transmittance: a thin film leads to better transmittance values, but implies a lower conductivity in comparison to a thicker one. Therefore, the optimization of optical and electrical properties consists in a compromise between the two and in an intermediate thickness. It is also important to notice that during the thermal annealing the film undergoes a mass loss, partly due to substituents desorption, partly because of an effective loss of graphene layers. We perform TGA measurements to trace these events, that can be partially con-

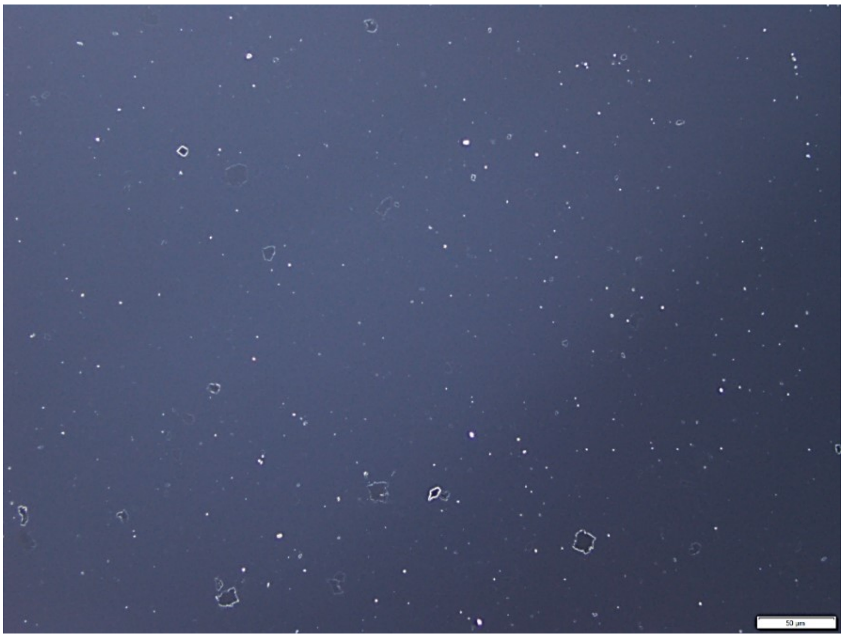

Figure 3.1: Dark field image of graphene oxide on quartz. The dark field enhances the edges of the flakes superimposed on the uniform film composed of few layers. The scale bar is of 50μm.

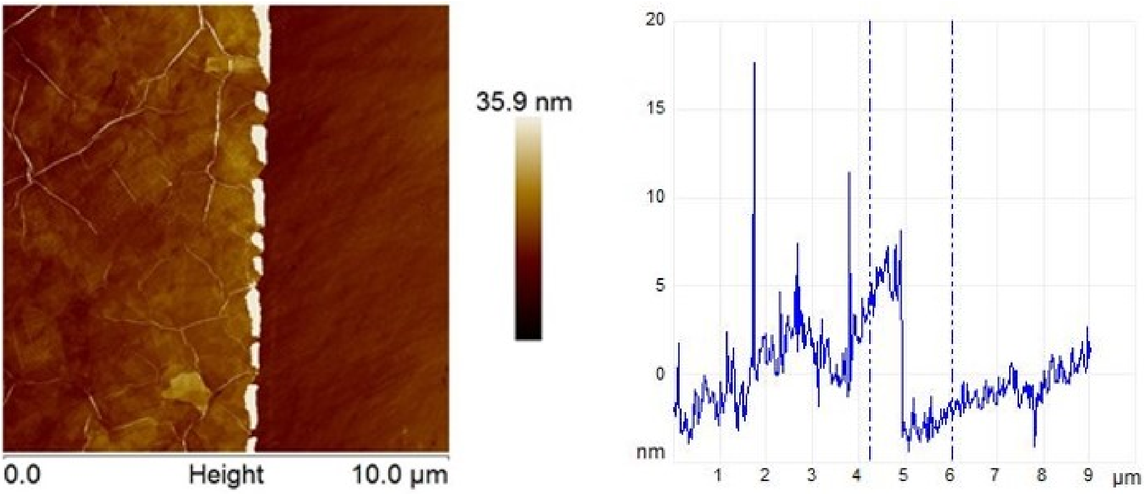

Figure 3.2: *Left* AFM image in tapping mode of Pristine GO film scratched on purpose to show the different morphology of film and substrate and to measure the film thickness. *Right* Height profile used to measure the film thickness.

trolled by the heating ramp used to reach the reducing temperature, but that cannot be completely avoided. Therefore, the analysis we make on the pristine GO film must take into account that the thickness of the film decreases during reduction. Finally, the correlation between the thicknesses of the film before and after reduction is an important instrument to optimize the deposition procedure according to the desired thickness of the reduced film. The data confirm this dissertation, being the mean thickness of GO on quartz samples equal to (6.4±2.5)nm and, after thermal annealing at 450°C for 3 hours, only (2.4±0.6)nm. This decrease in thickness is an evident sign of the mass loss already mentioned and a compacting of the layers.

Moving to Figure 3.3, we can notice that the film is continuous even at microscopic scale, since there is no evidence of the quartz substrate. In the AFM image of the pristine GO film (Figure 3.3, left) there are many creases, referable to the overlapping of the flakes, and their possible folding. The creases amplify the roughness of the film, but it is not clear yet if they can somehow influence the electric properties of the rGO. For the moment, we do not consider them when calculating the film roughness. Moreover,

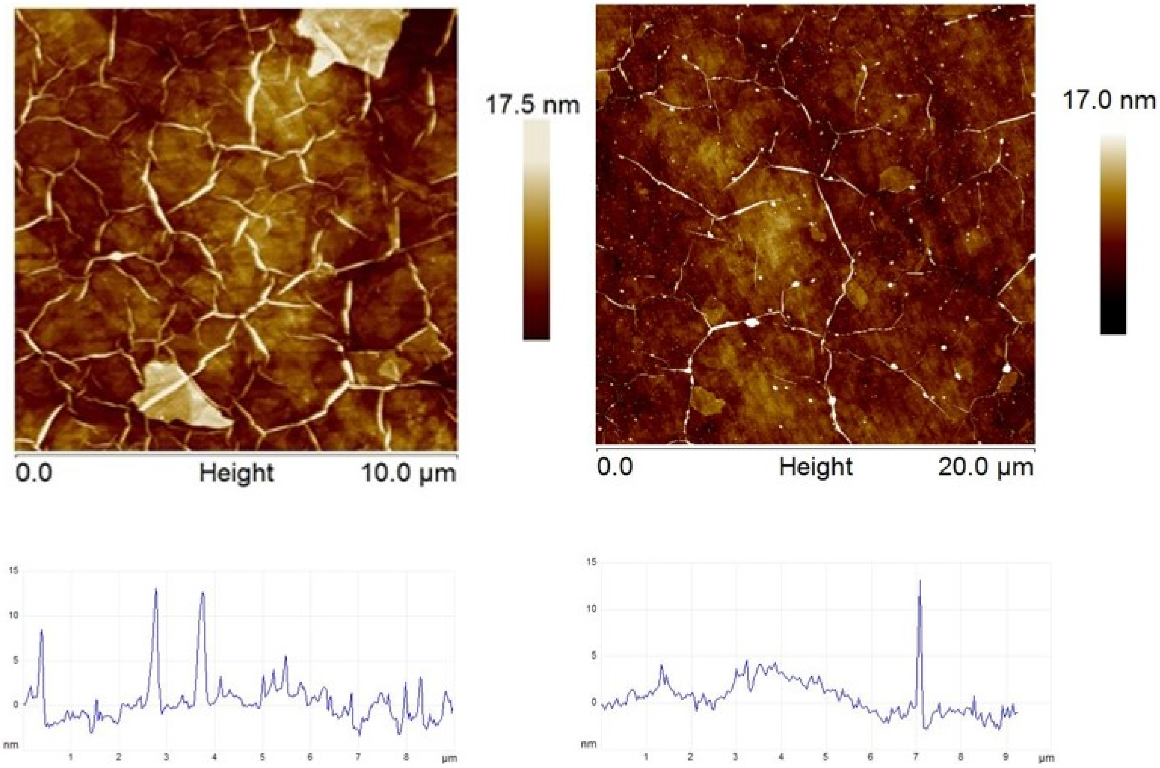

Figure 3.3: AFM images in tapping mode and relative height profile of: *Left* Pristine GO film imaged in the center of the sample, where the additional flakes and creases due to flakes folding are present; *Right* Thermally reduced GO film at 450°C for 3 hours.

the edges of the different flakes composing the layers are still distinguishable as sharp shadows, and this is a proof that the reduction has not took place yet. Indeed, we see in Figure 3.3 (right) that the reduced film presents a sort of fusion of the flakes edges that increases with the degree of reduction. Another consequence of the reduction is the presence on the film surface of small and randomly dispersed particles (white points in the image), probably residual products of the reduction. A better vacuum during the reduction, or a slower process, may minimize the dirt on the sample.

Considering the roughness values obtained with the same deposition technique, the mean surface roughness of our GO on quartz is R_a=(1.2±0.2)nm (arithmetic average) and R_q=(1.6±0.3)nm (root mean squared). An increase in thickness in the pristine GO film is correlated with a decrease in roughness, because of an averaging of the height variations of the flakes. This trend is in contrast with the conclusion of Becerril et al.[19] whose work is a landmark because of their excellent results. They individuate a positive correlation of thickness and roughness, while our is negative (see Figure 3.4). The explanation we give to this is the difference in the GO deposition procedure: they perform one single spinning of a more concentrated GO solution (4-8 mg/mL) that probably prevents a more compact flakes arrangement, which is instead possible with our double spin of a more diluted dispersion (1mg/mL). This explanation is endorsed by the direct comparison of roughness values: for a ~8 nm thick film, they report 2.2 nm R_q, while we have obtained approximately 1.4 nm R_q.

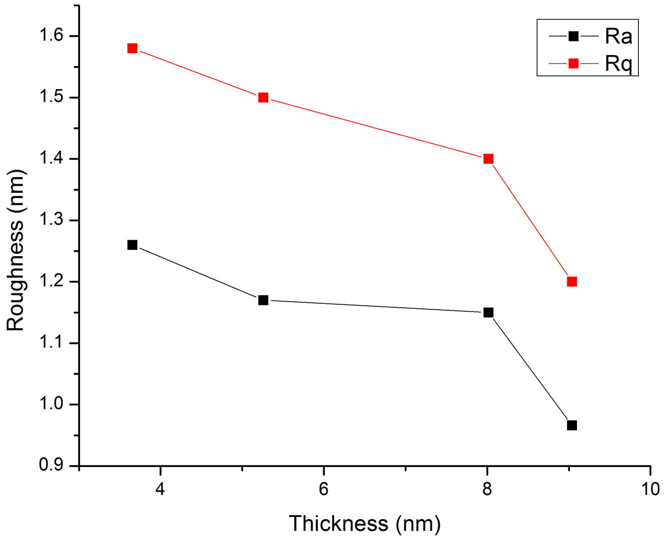

Figure 3.4: Thickness vs roughness of pristine GO film on quartz, obtained with the same deposition technique.

The roughness analysis of the reduced samples shows no more correlation with the thickness of the film, nor a defined trend with respect to the not-reduced one, but after reduction it decreases at the values of $R_a=(0.97\pm0.13)$nm and $R_q=(1.22\pm0.17)$nm.

3.2 XPS analysis

The XPS analysis of samples differing in reduction temperature is very important to understand how effective the reduction process is. We monitor the carbon region and what we expect is a progressive decrease of the carbon-oxygen peak, located approximately at 286 eV, in favor of the carbon-carbon one at 284.8 eV. The oxygen loss is indeed typical of reduction processes and the increase of the C-C peak indicates the progressive restoring of the honeycomb lattice and consequently the enhancement of the electrical properties of the film.

The samples we analyze cover the whole range of reduction temperatures we have tested (150°C, 250°C, 450°C, 550°C, 700°C, 1000°C) plus a sample of pristine GO. All the samples are reduced with the mentioned procedure for 2 hours, except for the 1000°C one, that with our setup could be reduced for 40 minutes maximum. The survey spectra taken over the full range of energies are usually useful to individuate the more intense peaks and, for rGO, to calculate the carbon-to-oxygen ratio. This is yet not the case, being the film so thin and the X-rays far more penetrating than the film thickness that the detected oxygen belongs mostly to the quartz substrate, whose chemical composition is SiO_2.

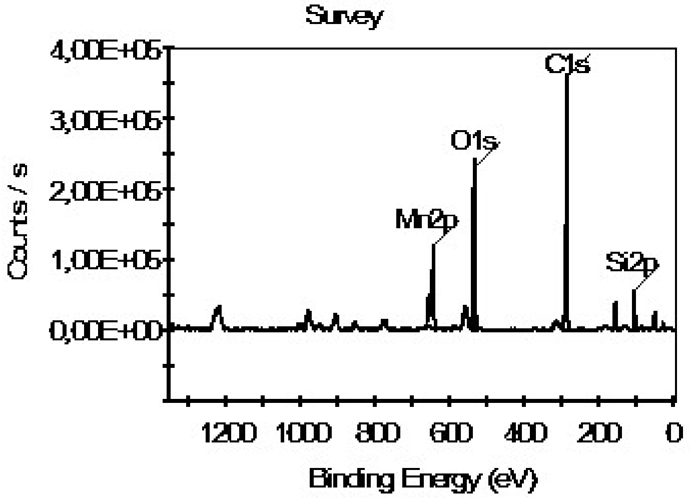

Figure 3.5: Survey XPS spectrum over the whole energy range of the instrument for a sample of rGO on quartz reduced at 1000°C for 40 minutes.

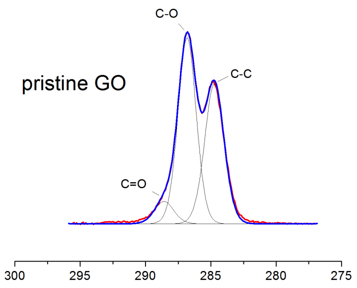

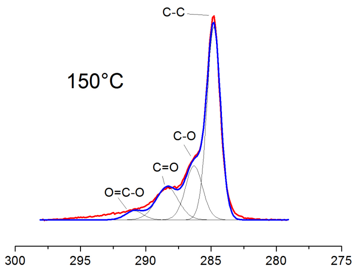

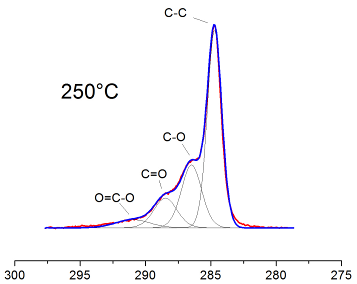

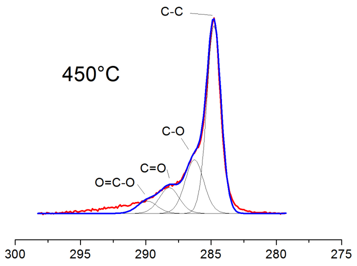

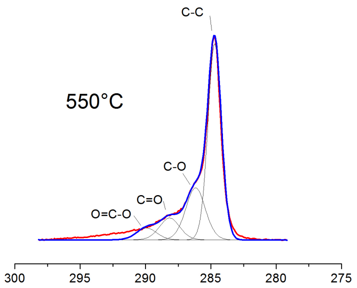

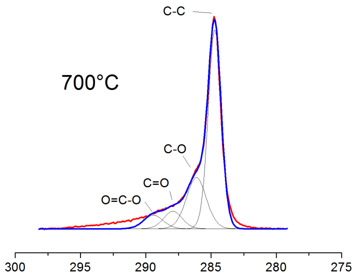

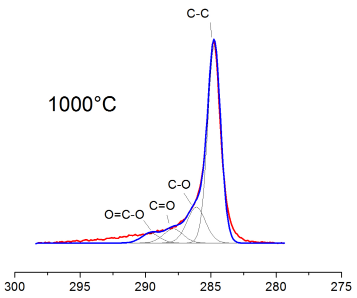

Figure 3.6: XPS spectra recorded on samples with different degree of reduction due to different annealing temperatures, from pristine GO to 1000°C rGO. Each graph reports both scanning line and envelope line of the postproduction analysis, together with energy and % area of the main peaks.
X axis: Binding Energy [eV].

This is confirmed by the fact that the silicon peak is intense too, around the 10% of the total composition (see Figure 3.5). We consider then the C1s spectra, one for each sample, which are reported in Figure 3.6. The analysis we perform consists in the deconvolution of the plot as to individuate the principal peaks of interest mentioned before. The carbon peak is naturally asymmetric; therefore, the high-energy tail is not unexpected. In Figure 3.6 is evident how the carbon-oxygen peak, even higher than the C-C one in the GO film, progressively reduces its height. This is even more evident in Figure 3.7, where the values of C-C percent peak area and C-O percent peak area trace two almost symmetric curves that depart progressively with increasing reduction temperature. Thanks to the XPS analysis, together with the evaluation of sheet resistance of the next section, we can select a narrower range of temperatures worth to be investigated further for better results.

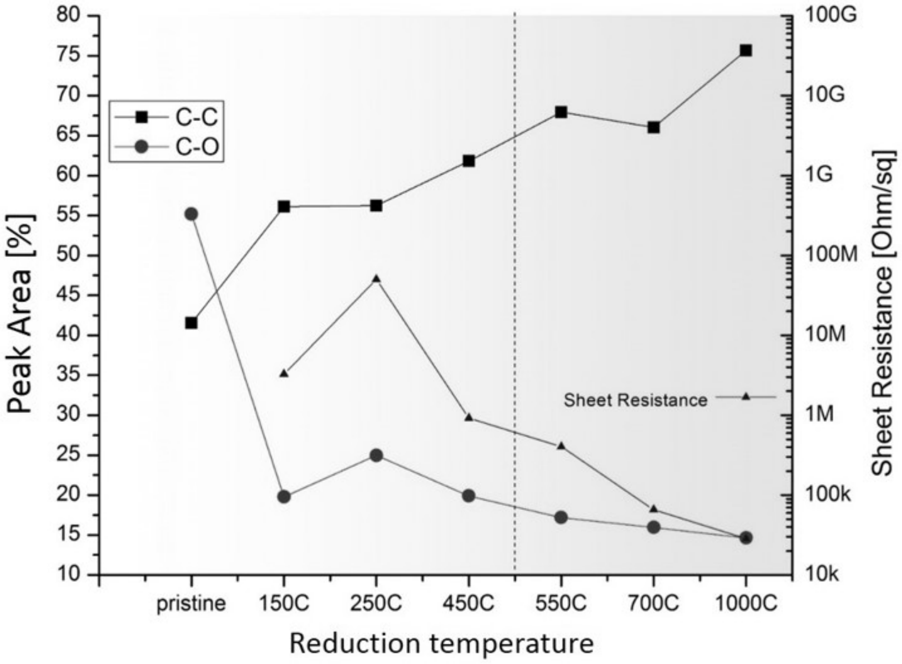

Figure 3.7: Comparison of the percent areas of C-C (squares) and C-O (circles) peaks of rGO films at different reduction temperatures, together with their sheet resistance values (triangles).

3.3 Sheet resistance

Since our principal goal is to have a well conducting film, the sheet resistance is a fundamental evaluation parameter. What we expect to see is its decreasing with increasing restoration of the carbon-carbon bonds of the lattice. As said, one of the indicator of the progressive restoring of the honeycomb lattice is the decrease of the carbon-oxygen peak area of the XPS analysis with reduction temperature and therefore the sheet resistance should have similar behavior. This expectation is confirmed observing Figure 3.7, where XPS data on C-O peak area (circles) and sheet resistance data (triangles) have a perfect accordance.

However, the sheet resistance data presented in Figure 3.7 are but a restricted example of the values we measure over the full range of reduction temperatures and times we test. The values of unreduced GO film are the highest, exceeding $G\Omega/\square$ and the limit of the instrument, the more poorly reduced samples have sheet resistance values of $10^7\Omega/\square$, while the best performances reach the order of tens of $k\Omega/\square$.

From the collected data, the sheet resistance values are lower at higher annealing temperatures, more effective at removing the oxidizing groups, while the correlation between sheet resistance and reduction time is not so well defined. For low reduction times, up to 3 hours, the sheet resistance decreases with increasing time. Longer reduction times, however, lead to a worsening of the conductivity performances, probably because of an excessive thinning of the film. TGA measurements confirm this mass loss during the dwelling, when the final annealing temperature is kept constant. This hypothesis is strengthened by the optical transmittance measurements that are discussed in the following section.

The heating process is another factor that influences the sheet resistance, since the delicate diffusion of the gases that evolve during the reduction can turn into exfoliating pressure, if the process is too fast. This can be avoided slowing down the heating around the critical temperature, improving the electric performances. The individuation of this critical point and a complete analysis of the heating process by TGA is presented and commented in Section 3.5.

Since the sample fabrication is quite time demanding, mostly because of the long reduction and cooling times, from now on we will optimize the production reducing the samples at 550°C, 700°C and 1000°C only. Indeed, as shown in Figure 3.7, these sample have sheet resistance lower than $1M\Omega/\square$: higher values are inadequate to compete with the conductivity values already reached with graphene oxide, which are of the order of magnitude of $k\Omega/\square$.[19 29]

It is interesting to point out that sheet resistance values are almost unaffected during the transfer process that allows to move the reduced films from the quartz or Si/SiO_2 substrate, necessary for the high temperature reduction, to the flexible one, such as PET. The transfer method, described in Section 2.6, leads to flexible samples with sheet resistance of the same order of magnitude they had before transferring, indicating that nor the process, nor the eventual KOH residuals, nor the substrate influence the electrical performances of the rGO films. The preliminary results in terms of sheet resistance of the transfer method are shown in Table 3.1.

Si/SiO_2	PET
$(28 \pm 9)k\Omega/\Box$	$(78 \pm 15)k\Omega/\Box$
$(27 \pm 2)k\Omega/\Box$	$(76 \pm 18)k\Omega/\Box$

Table 3.1: Sheet resistance values of rGO film before and after being transferred from Si/SiO_2 substrate to PET substrate.

3.4 Transmittance

We perform transmittance measurements to test the goodness of our films for applications requiring transparency and to individuate an eventual transmittance dependence from the reduction parameters. Actually, from the recorded spectra we can also monitor if the reduction has taken place. As it is shown in Figure 3.8 (left), if we compare the spectra of pristine GO film and rGO film, the second shows a redshift of the absorbance peak during the reduction, from 228nm to 275nm. This shift is due to the partial restoring of the aromatic C-C bonds, since the peak is ascribed to their $\pi \rightarrow \pi^*$ transition.[67] The peak should progressively right-shift while the reduction is becoming more effective, and in theory we should be able to monitor the degree of reduction observing the position of the peak.

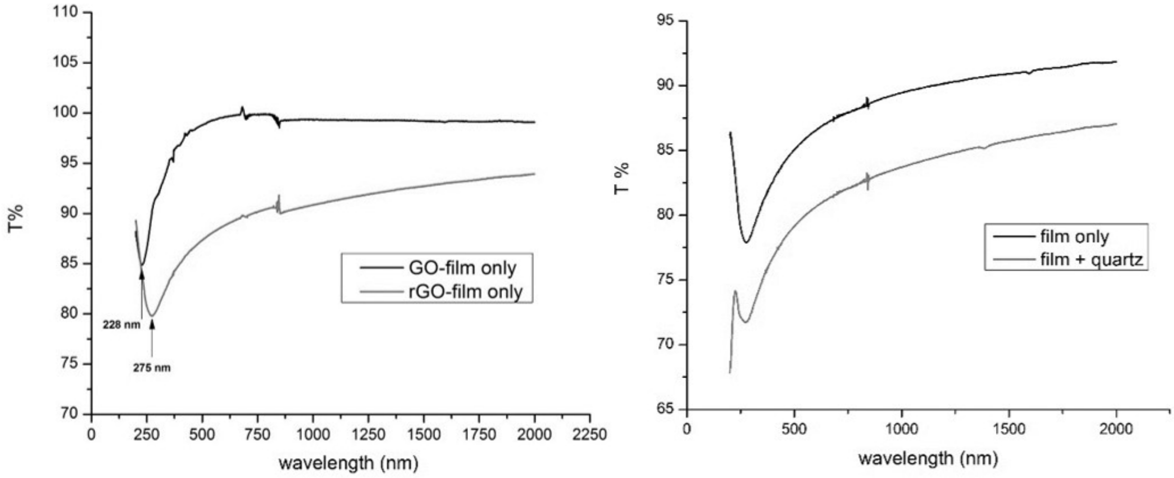

Figure 3.8: *Left* Comparison of transmittance spectra of pristine GO film and 450°C-3 hours reduced GO film. These data have been acquired with reference to quartz, so they refer to the film only. *Right* Comparison of the spectra of the same sample, measuring only the film (black line) and the ensemble film + quartz substrate (grey line). The rGO has been annealed at 700°C for 2 hours.

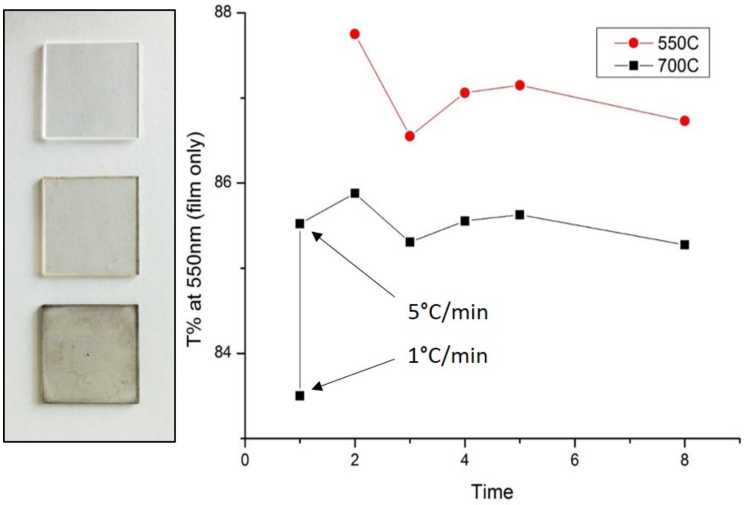

Figure 3.9: *Left* Sequence of a clean quartz substrate (top), a GO film on quartz (center) and a rGO film on quartz annealed at 1000°C for 40 minutes (bottom). *Right* Transmittance at 550nm of rGO films annealed at 550°C and 700°C for 1,2,3,4,5 and 8 hours.

Our is but not the case, probably because the steps of the reduction temperature are not gentle enough.

During the reduction, the film becomes darker and we can see naked eyed the decrease in transmittance also revealed from the spectra analysis (Figure 3.8, left and Figure 3.9, left). From the collected data, we measure a decrease of more than 10% in transmittance at 550 nm and this is a common result for all the samples considered. Nevertheless, the T% values are always above the 75% in the whole 200nm-2000nm range. Since the measurements reported until now have been done with a double-beam spectrophotometer with a clean quartz substrate as a reference, they refer only to the film and are independent from the substrate. However, for future application it is important to evaluate the performances of the whole assembly composed by film and substrate. Looking at the spectra of Figure 3.8 (right), which refer to the system quartz+film reduced at 700°C for two hours but are exemplificative for all the samples, we notice that the transmittance of the quartz+film configuration, measured in the peak, is around 8% lower than the one measured for the film alone. Anyway, despite to the quartz absorbance, the transmittance values never go under the 7% in the range between 230nm and 2000nm. Compared to the works presenting the best performances, this is a good result.[19 29]

After the selection of the best reducing temperatures in Section 3.3 according to sheet resistance values, we now proceed investigating the selected temperatures of 550°C and 700°C more in detail, performing reduction lasting 1, 2, 3, 4, 5 and 8 hours and evaluating the relative transmittance values. The results of transmittance at 550nm are reported in Figure 3.9 (right). We can notice that, after an initial decrease of the transmittance from 2 to 3 hours annealing, according to the expected darkening of the reduced film, the measured values increase again from 4 hours annealing. We interpret this behavior as consequence of film loss during the process, probably because of an excessive exposure to high temperatures. For this reason, we decide to set the maximal reduction time at three hours.

Moreover, from the same graph we can see a huge difference of absorbance between two samples, whose reduction processes differ only for the speed of the heating: the one heated at 1°C/min has a transmittance of more than 2% lower than the sample heated at 5°C/min. The hypothesis is that a slower heating process can reduce the film exfoliation during the annealing, leading to lower transmittance values but, eventually, better conductivity.

3.5 ThermoGravimetric Analysis

We perform ThermoGravimetric Analysis (TGA) on GO powder with different heating speed and temperature settings to evaluate more in details the mass loss that the films undergo during reduction. The three experiment we perform are: final temperature 550°C, heating at 5°C/min; final temperature 700°C, heating at 5°C/min; final temperature 700°C, heating at 1°C/min. As we can see from Figure 3.10 (on the left TGA, on the right its first derivative, DTG), independently from the parameter setting, the GO powder has the same general behavior, characterized by a consistent mass loss of ∼25% over a temperature range of approximately 75°C. The curves with the same heating ramp are obviously behaving in the same way, with the slight differences attributable to differences in the GO powder preparation. The curve with slow heating ramp, instead, presents the flex of the rapid mass-loss process at lower temperatures (171°C instead than 191°C). This is reasonable because a slower heating leads to a bigger heat accumulation.

To understand the origin of the mass loss, we refer to the work of McAllister et al.,[68] who have studied and modelled the graphite exfoliation process. Thanks to their results, we can individuate the minimal requirement to limit the mass loss due to exfoliation during reduction. They evaluate, as we do, the TGA curve of GO samples and at the same time they perform an FTIR scan of the gas evolved during reduction (see Figure 3.11). They individuate the products of the reduction as CO_2 and H_2O, which, if developing rapidly because of a fast heating rate, have no time to diffuse between the layers of the film and create therefore a pressure sufficient to induce exfoliation. The limit they set to the heating rate is 1°C/min: at this rate or lower, exfoliation is avoided.

An entire reduction process with heating rate 1°C/min is yet time demanding and, once the critical temperature range for exfoliation has been passed, it is convenient to reach the annealing temperature as fast as possible. Thanks to further measurements with TGA, we determine the exact start and end point of the rapid mass loss, once we

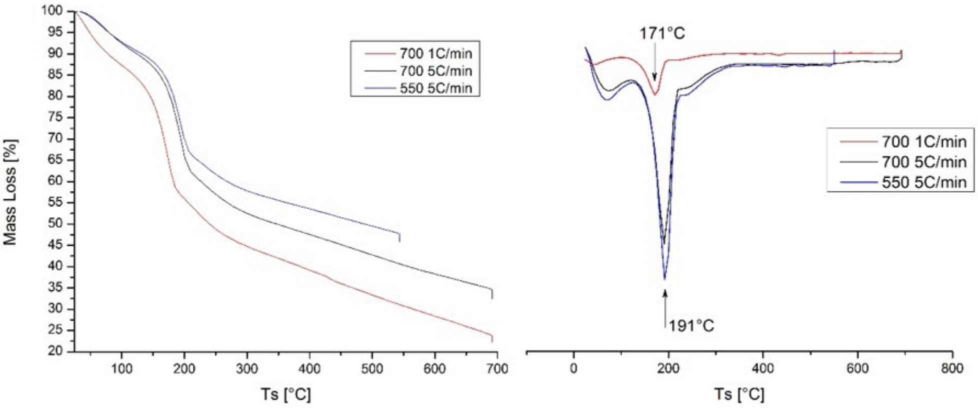

Figure 3.10: TGA spectra (*left*) and DTG spectra (*right*) of GO powder during reduction with different parameters settings: *blue* final temperature 550°C, heating at 5°C/min; *black* final temperature 700°C, heating at 5°C/min; *red* final temperature 700°C, heating at 1°C/min.

have set the room temperature as initial temperature of the annealing and 20°C/min as initial heating rate. The rapid mass loss boundaries are found to be around 150°C and 200°C respectively and between these temperatures, we set the heating rate at 1°C/min, while once passed the 200°C the heating rate can rise to 50°C/min. This parameters configuration guarantees minimized exfoliation during reduction and optimized time demand of the process.

Appling this optimized heating process, the improvement of the performances of the film is great. The conductivity of the samples increases up to three order of magnitude (see Figure 3.12) and the compromise for this is a transmittance of no more than 1% lower than the previous one, with values at 550nm always well above 84% and minima over 75%, for films reduced at 550°C and 700°C. The best result in terms of electrical conductivity is the one obtained at 1000°C for 55 minutes, which has a sheet resistance of (19±1) kΩ/□ and transmittance values of 82,9% at 550 nm and 72,9% in the minimum.

3.6 UPS data analysis

Since for many applications it is important to know the work function of the rGO film, for example if we want to integrate it in solar cells, where its work function has to match with those of the other components, we perform UPS measurements on different samples. The results we obtain are shown in Figure 3.13.

The reported data are an average over three measurements in different spots of the sample, each. The set of data for each sample contains values consistent with one an-

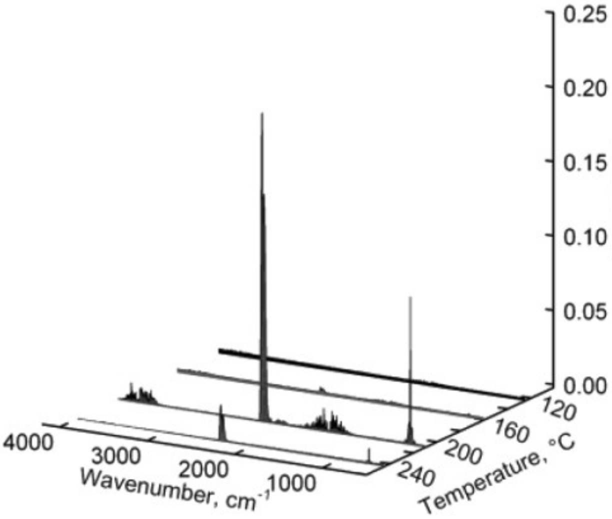

Figure 3.11: CO_2 (wavenumbers 2360 cm^{-1} and 690 cm^{-1}) and H_2O (wavenumbers 1340-1900 cm^{-1} and 3550-4000 cm^{-1}) just after the onset of rapid mass loss (here at 210°C). This indicates that decomposition of the oxygen-containing functional groups, rather than vaporization of intercalants, causes the exfoliation.[68]

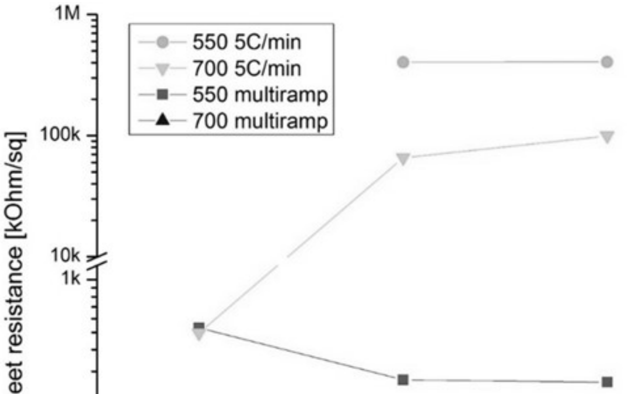

Figure 3.12: Comparison of the sheet resistance values obtained for the same annealing temperature, but different heating rate, in particular the constant rate of 5°C/min vs the multiramp of 20-1-50 °C/min and changing temperatures of 150°C and 200°C.

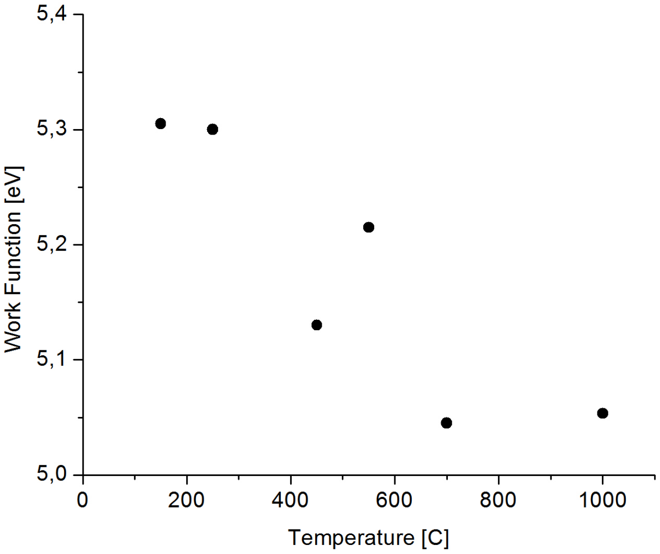

Figure 3.13: Work function values of rGO films as function of reduction temperature, measured by UPS.

other. The data show a well-defined trend consisting in a decrease of the work function of the film together with the increase of the degree of reduction (and the reduction temperature). The trend is favorably oriented toward the work function of graphene, which is of ∼4.62 eV.[69] This is a positive indicator of the effectiveness of the reduction process that aspires to a complete restoring of the graphene properties.

3.7 Electrical characterization

The electrical characterization of the bottom-gate field-effect transistors (made of rGO on Si/SiO_2 substrate with gold electrodes on top) is done monitoring the source-drain current (I_d) while a sweeping gate voltage is applied. The measurements are performed in air. We first notice that there is a linear, positive dependence between V_d and I_d. We also monitor the gate current: it is desirable to have it as low as possible as not to influence the source-drain one. Having a meaningful gate current means that the dielectric, here 230nm of SiO_2, is broken, maybe because of the annealing, or that the current flows through the edges of the sample, and the current we want to measure (the one through the rGO film) is instead corrupted by the current flowing through the well conductive silicon substrate. After the optimization of the device fabrication process, where the sample is cleaned at the edges before the annealing, the gate current we measure is of

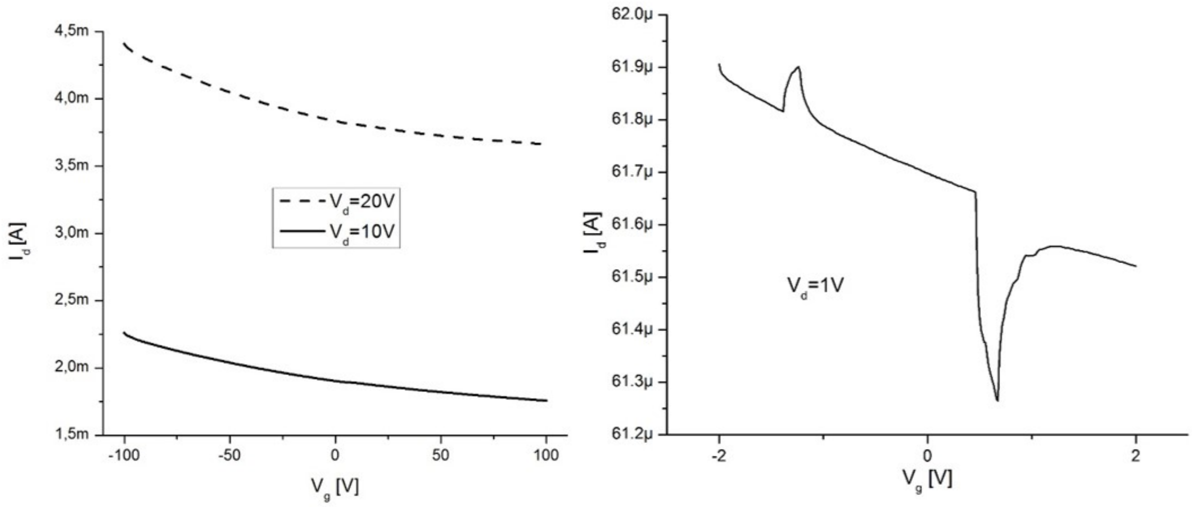

Figure 3.14: I_d-V_g curves of the three terminal devices of rGO on Si/SiO_2 substrate with gold electrodes. *Left* Source-drain current under high drain bias, with varying gate voltage. The Dirac point of the rGO can not be seen even over a large gate range and the curves indicate a positive doping of the film. *Right* The electrical behavior of the device is tested in air and the drain current is affected by nitrogen flow (positive peak on the left) and flow of H_2O vapor (negative peak on the right).

the order of tens of nanoampre over the whole range of gate and source-drain bias we apply and, most important, it is three or four orders of magnitude smaller than I_d.

The expected behavior is a symmetric curve with its minimum (V_g^D, Dirac gate voltage, where the carriers change from electrons to holes) at a gate of 0V and a kind of parabolic shape.[49] The wider the amplitude of the curve, the higher the impurities of the carbon lattice of the film.[70] The initial range of the gate values is chosen according to literature,[49] then increased to find the Dirac point, which cannot be found in the initial ±20V gate voltage range. All the IV recorded, up to a maximum gate range of ±100V (see Figure 3.14, left), show a shift toward positive voltages that prevents the Dirac point from being in the screened gate bias range. This shift can be related to the high density of charged impurities either in the substrate or in the vicinity of rGO,[70] less likely to a positive doping of the film through the reduction process or the substrate. The first hypothesis is strengthened by the amplitude of the curve.

The devices also show a sensing behavior for both nitrogen and water vapor, as visible in Figure 3.14, right. The positive peak on the left of the graph is induced by nitrogen flow directed toward the device during the measurement, while the negative peak is due to water vapor flow. This sensing behavior of rGO is not unexpected,[71][72] but instead of studying more deeply this feature of our devices, which is out of our focus, we take advantage of this experimental proof of the effects of humidity on rGO-based field-effect transistors to set that the following measurements will be performed under controlled atmosphere of nitrogen. Indeed, the water vapor present in the air can affect the I_d current, resulting in underestimated performances of the device. The nitrogen flow, instead, more than doping the rGO film, contrasts the effect of the humidity, leading to better performances in terms of measured current per applied gate voltage, but with no permanent effect.

3.8 Rhodamine 6G doping

We perform again the electrical characterization of the devices, this time to test the effect of Rhodamine 6G doping on rGO film. Actually, before measuring, we dropcast a solution of Rhodamine 6G in methanol on the film in correspondence with the top electrodes we are going to contact. What we expect to see is a negative doping effect on the rGO because of the R6G[44] and consequently a negative shift of the curve that possibly brings the Dirac gate voltage inside the scanned gate range.

The expectations are fulfilled, as Figure 3.15a shows: the Dirac gate voltage is left-shifted from an unknown value to approximately 10V and its value is independent from the source-drain voltage. The presence of R6G does not modify the linear dependence of the I_d current from the source voltage (insight of Figure 3.15a), meaning that the doping is not related to the current flowing in the channel. Nevertheless, the electron donation influences the curve shape, whose left side, corresponding to the regime in which the charge carriers are the electrons, has an higher slope (higher carriers mobility) compared to the right side of the curve. This is particularly evident in Figure 3.15b. If the sample is left in air, with R6G dropcast on it, the doping is partially lost, as you can see from the blue curve of Figure 3.15b, recorded five days in air after the dropcasting. This can be due to the deterioration of the rGO film, which absorbs charged impurities that have the effect of a positive doping, together with a lowering of the carriers mobility,[70] contrasting the negative doping of the R6G.

An additional negative shift of the IV curve is possible if the Rhodamine 6G is irradiated with green light at 530nm, where the dye has its maximum of absorbance. We place a LED of the right wavelength very close to the sample, without collimator, and we monitor the change in the Dirac gate voltage position. We expect a negative shift because graphene is known to quench R6G fluorescence via electron transfer, with direction from the dye to rGO.[46] This is verified in Figure 3.15b, where the blue curve recorded before irradiating shifts negatively of 20V as soon as the LED is turned on (red curve). Once the LED is turned off, the device shows no evidence of recovering to the pristine electron density. In fact, the red curve of Figure 3.15b and the black one of Figure 3.15c, taken at two hours of distance, present the same position and shape. To

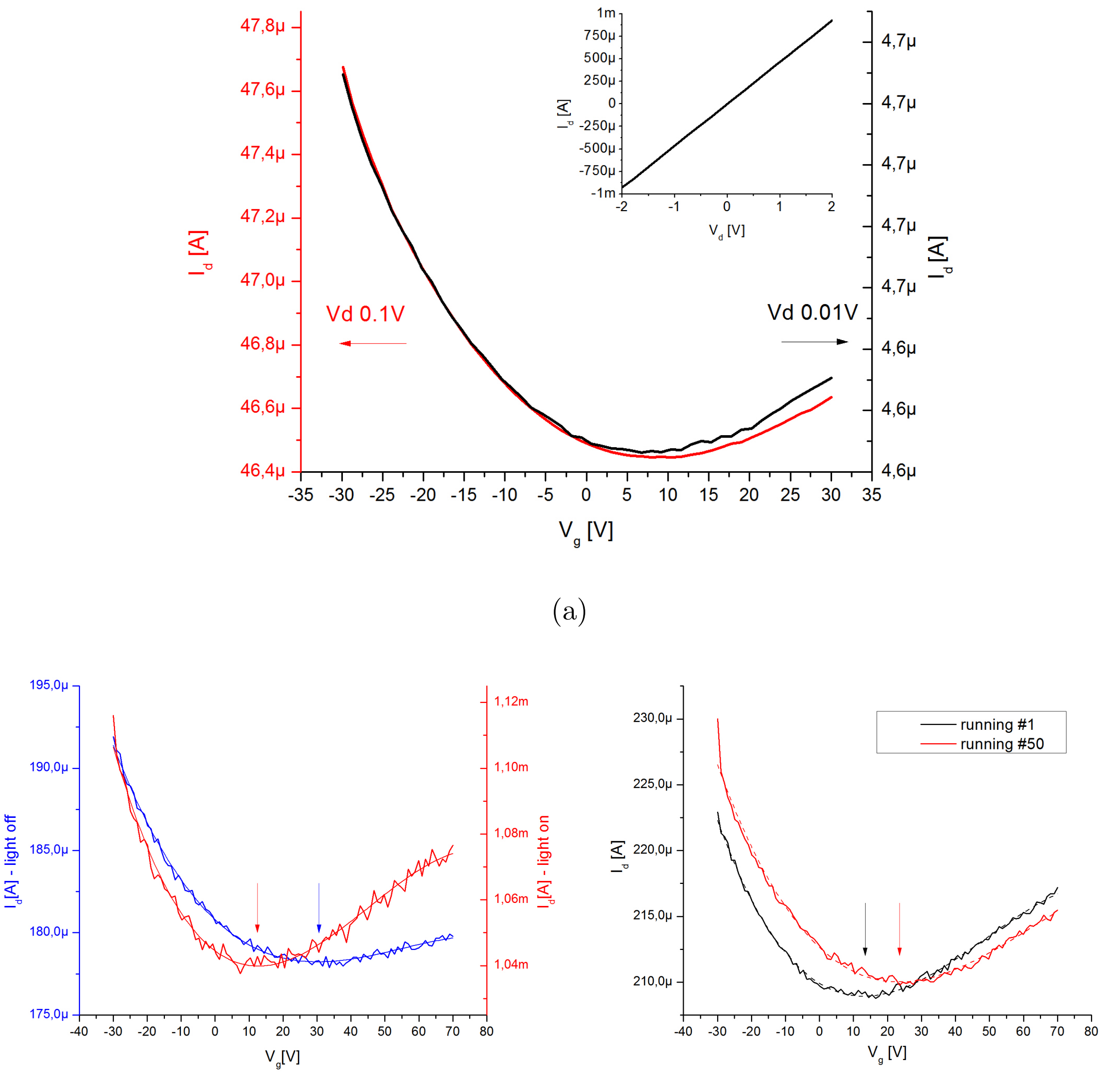

(a)

(b) (c)

Figure 3.15: IV curves of rGO doped with Rhodamine 6G. (a) IV curve recorded on rGO-based field-effect transistor doped with Rhodamine 6G, showing a negative shift respect to the undoped curve and the appearance of V_g^D around 10V. (Inset) I_d vs. V_d, which are linearly proportional. (b) IV curve recorded on rGO-based field-effect transistor doped with Rhodamine 6G, before (blue) and during (red) irradiation of the device with green LED light at 530nm (absorbance peak of R6G). The V_g^D is further right shifted, from around 30V to 10V. V_d=5V. (c) After irradiation, the IV does not shift spontaneously back to the values before irradiation (black curve). It takes a 50 times repetition of the measurement to restore the initial values (red curve). V_d=1V.

restore the device to the situation of no electron trapping, we have to induce the electron releasing via current flow through the channel. Therefore, we repeat the measurement fifty times in a row to see a progressive right-shift of the V_g^D, back to the value obtained with simple Rhodamine 6G dropcasting. Between the first and the fifth measurement running, we measure a positive shift of approximately 10V (see Figure 3.15c).

Summarizing, the ability of R6G of negatively dope the graphene, together with the quenching of Rhodamine 6G fluorescence by rGO via electron transfer, create a sort of double step doping for our device. The first negative shift is obtained by simple R6G dropcasting, it is stable under controlled atmosphere and can be reversed by washing the Rhodamine away from the sample with ethanol, which is safe for the rGO film. The second negative shift, equally intense as the previous one, can be induced irradiating the dye with light at 530nm and reversed letting the current flow through the channel.

3.9 Mechanical characterization

Every time we try to completely remove an area of the reduced film scratching it away, we note that this process is never fully successful, so that there is still a percolation path in that area, and the current flows through it. This strange behavior, this hardness of the film once reduced, make us want to evaluate the elasticity of our rGO films. The literature presents few results about Young modulus for graphene and graphene derived materials, and in particular the publishing report a low value for chemically reduced GO Young modulus[73] compared to that of graphene.[74] Because of the given data, the comparison between the two sources can be done only through their 3D Young modulus values, the results of the conversion of the 2D Young modulus for bulk materials. The values are (185±58) GPa and (1.0±0.1) TPa for chemically reduced GO and graphene, respectively.

To test our thermally reduced graphene oxide films, we follow the same procedure used for graphene by Lee et al.[74] based on AFM nanoindentation and recording of force-displacement curves. The difference between our work and the reference is that we have films instead of single flakes, which is a good assurance of no slipping of the membrane on the substrate while measuring. With this method, we can obtain the 2D Young modulus of each membrane, mediated on all the recorded force-displacement curves for the same membrane, and the displacement and force values at the breaking point of the film.

The measurement required to extrapolate the 2D Young modulus is a force vs. displacement curve, recorded on a suspended rGO membrane obtained via film transfer on a patterned substrate, as explained in Section 2.6. This measure is more reliable if performed in the center of the membrane, therefore a surface scan precedes the tip positioning in the point selected for the measurement. Not to risk having the membrane broken, we perform the survey scan in tapping mode. A typical image acquired during the survey scan is shown in Figure 3.16, from which we can select an integer membrane

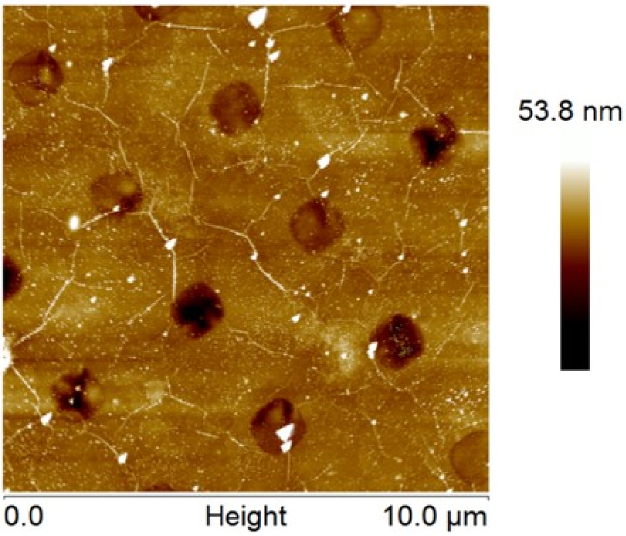

Figure 3.16: AFM image of the patterned substrate with the rGO film on top.

and position the tip in its center. The choice of the AFM tip must be adequate for our purpose: high elastic constant of the cantilever to assure a good tapping scan and to be able to push hard enough against the membrane, hard tip, and good cantilever reflection for a better response of the photodiode. We choose a Non-Contact/Soft Tapping Silicon Tip with elastic constant of 41N/m, whose values are given by the constructor and taken as reliable. We measure only membranes suspended over wells with 1m of diameter, the only ones almost circular.

We always take a preliminary force curve on a clean quartz substrate, assumed as completely rigid, to extrapolate the elastic constant of the system Tip+Air+Water film present on top of the sample. We obtain an elastic constant of 39.3N/m that will be further used in all the membranes measurements instead of the 41N/m elastic value of the cantilever only.

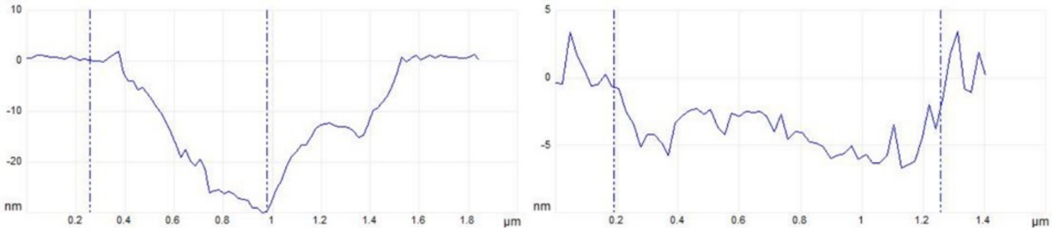

Figure 3.17: *Left* AFM profile of an empty well; triangular shape. *Right* AFM profile of an rGO membrane suspended on the well; there is a few nanometer adhesion of the film at the walls.

During the survey scan, we can roughly identify the integer membranes with respect to the empty wells because of the profile: the membranes, as in Figure 3.17 (right), adhere at the walls for 2 to 4 nm and are almost flat in the middle. The empty wells, instead, are very deep and the tip cannot properly follow their profile, resulting in a triangular shape (see Figure 3.17, left).

We perform the analysis of the curves following the model proposed by Lee et al.[74] First of all, we must be able to assume that our rGO film can be modeled as a 2D membrane with zero bending stiffness and this is reasonable because of the almost complete reduction by thermal annealing of GO, that makes it very similar to the graphene. Moreover, we suppose the force-displacement curve to be independent from tip radius, if R<< a (a=membrane diameter), and from indenting tip position, if it's within $a/10$ of the center of the film. With these premises, the system can be thought as a clamped circular membrane, made of linear isotropic elastic material, under central point loading. Following Lee's model,[74] we can approximate the force-displacement behavior as:

$$F = \sigma_0^{2D}(\pi a)\left(\frac{\delta}{a}\right) + E^{2D}(q^3 a)\left(\frac{\delta}{a}\right)^3$$

Where F is the applied force, δ is the deflection in the central point, σ_0^{2D} is the pretension of the film, E^{2D} is the 2D Young modulus we want to know, q=1/(1.05-0.15σ-0.16σ^2) a dimensionless constant dependent on the Poisson's ratio σ. About this last parameter, defined as ratio between axial compression and transversal strain of the film, the difficulty of obtaining it for rGO is about having no bulk material on which we can measure significant compression and strain at the same time. One more time, we will refer to the value used for graphene, that is actually the one for the basal plane of graphite,[75] because no references for rGO exist, there are some for GO, but they are the result of simulations and in any case the rGO structure is closer to the graphene one than to the GO one. Finally, the diameter a of our membranes is of 1μm.

Before the fitting, some correction to the as-taken curve must be done, as you can see in Figure 3.18. First of all, the force-displacement curve is plotted from the software with the displacement related to the Z motor of the AFM and therefore we must find the offset point after indentation at which force and membrane deflection are both zero. This point becomes the origin of our Cartesian axis. We choose as offset the point after the indentation with better alignment with the baseline, as to be sure to have zero force. The high noise level is treated with the smoothing tool of Origin software. Second, we must subtract the cantilever stiffness from the curve or, in our case, the stiffness of the system cantilever+air+water film that we have estimated on quartz, as explained before.

The curve so processed can now be fitted with the previous equation. We report here the 2D Young modulus results concerning five different membranes, each tested many times before breaking. For some of these membranes, we are also able to refer the data relative to the breaking.

If we compare the reported values with the 2D Young modulus of single layer graphene[74] equal to (340±50)N/m, we immediately note that the values for few layers of thermally reduced rGO are one order of magnitude higher than the graphene one. Moreover, the few data relative to the breaking point of the membranes indicate that the rGO film, even if only few nanometers thick, can stand a considerable force before breaking, and even higher pressure, considered the 7nm radius of the AFM tip.

Membrane	**Number of curves recorded**	**2D Young modulus [kN/m]**	**Breaking point displacement**	**Breaking point force**
1	8	4,7±0,6	153.516 nm	2.984 μN
2	3	3,7±0,3	128.126 nm	2.1202 μN
3	7	2,3±0,3	/	/
4	7	3,7±0,4	/	/
5	9	1,5±0,14	/	/

Table 3.2: Results of the mechanical characterization of five different membranes, consisting in their 2D Young modulus, and displacement and force at the breaking point.

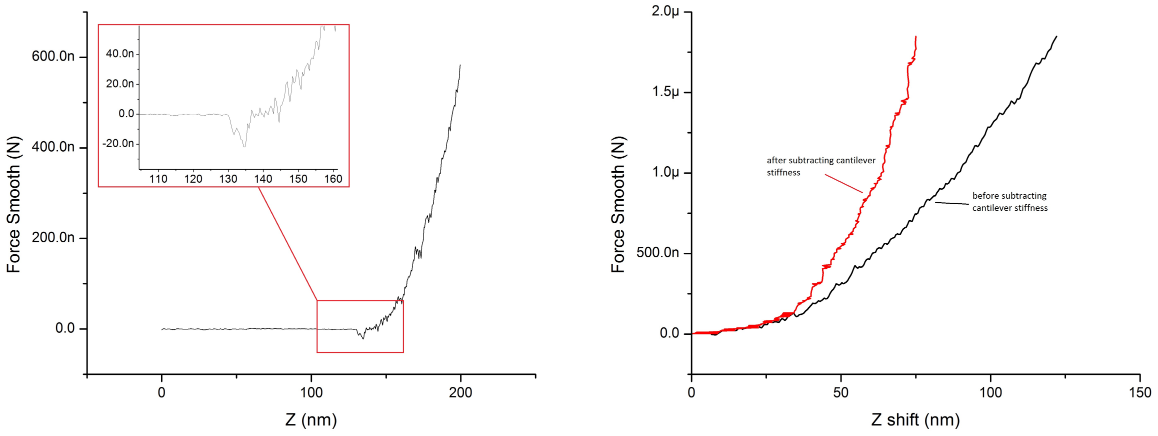

(a) (b)

Figure 3.18: (a) Force-displacement curve where indentation negative peak is underlined, before offset correction. (b) Comparison between force-displacement curves before (black) and after (red) subtraction cantilever stiffness.

Conclusions

In this thesis, we wanted to optimize the reduction process of graphene oxide films via thermal annealing, focusing on electrical conductivity and optical transmittance, and to study the electrical and mechanical properties of the rGO films according to their degree of reduction.

The film we used were deposited from one part of aqueous dispersion of graphene oxide diluted with three parts of ethanol via spin coating on quartz or Si/SiO$_2$ substrates. The particularity of ethanol dilution has allowed us to perform further deposition on dry films as controllable method to increase the film thickness. This deposition technique not only has led to uniform films over the whole substrate area, as proven both via optical and atomic force microscopy, but has also had consequences on the roughness of the film, that we found to be inversely proportional to the film thickness. One reason for this correlation can be the concentration of graphene oxide in the deposited solution (1mg/ml), which being so low allowed the GO flakes to rearrange during the deposition, particularly when spin coated on a dried GO film, as to minimize the surface roughness. The mean square roughness of our films is Rq=(1.64±0.3)nm, while their mean thickness before reduction is t=(6.4±2.5)nm. After the reduction, the average film thickness decreased, becoming (2.4±0.6)nm for 3 hours reduction at 450°C. We found that the thinning of the film was both intrinsic in the reduction process, because of the graphene layers that can become more compact, and heating ramp dependent, because a fast heating process can lead to exfoliation. Anyway, after reduction the correlation between film thickness and roughness is lost.

We performed the reduction of the GO samples on quartz on a wide range of temperatures and for different times for an initial overview, thanks to which we could do a selection of the best reduction parameter to have optimal sheet resistance and optical transmittance values. Via XPS analysis, we verified the proceeding of the reduction with increasing annealing temperature, monitoring the decrease of the C-O bond peak in favor of the carbon-carbon one, which increased with the progressive restoration of the lattice. We proved the values of the sheet resistance of the analyzed samples to be in good accordance with the results of XPS analysis and thanks to these two set of values (sheet resistance and atomic percentages of the carbon bonds) we were able to select the more promising reduction temperatures, which were found to be 550°C or higher. A further restriction of the reduction parameters range happened thanks to the analysis of the UV-visible-NIR spectra, obtained from the samples on quartz with a double beam spectrophotometer. The optical transmittance values, which should decrease with proceeding reduction because the film is known to darken when reduced, increased instead if the film was exposed to high temperatures for a long time. This indicated an undesirable thinning of the film; therefore, we set the maximal annealing time at 3 hours. We also noticed that the heating ramp influenced the optical transmittance values, in particular a slower ramp led to lower transmittance, index of a better reduction. We investigated further this experimental evidence with ThermoGravimetric Analysis, which helped us to individuate a critical temperature range in the GO reduction process, during which there were developed residual gases such as CO_2 and H_2O that could exert an exfoliating pressure on the upper layers of the film. Therefore, to avoid exfoliation, we simply kept the heating ramp at slow rates during this critical temperature range (between 150°C and 200°C) and we fastened it up before and after, to reduce the time demand of the reduction process. Comparing the results obtained with this multiramp approach with those given by a constant heating ramp, we had an improvement in sheet resistance of three orders of magnitude, while the optical transmittance suffered a feasible lowering of only 1%. Our best result ever has been the one obtained with the multiramp heating, final temperature of 1000°C for 55 minutes annealing, presenting values of sheet resistance of $(19\pm1)\mathrm{k}\Omega/\square$ and of optical transmittance equal to 82,9% at 550nm and 72,9% in the minimum of the spectrum.

Further investigation of the material properties went through UV photoelectron spectroscopy to evaluate the work function of rGO in dependence of the reduction temperature. The evaluated work functions diminished with increasing reduction temperature and the trend was favorably oriented toward the work function of graphene, which is of ~4.62 eV.

The electrical characterization of the film under gate bias has been possible after the realization of bottom-gate top-contact field-effect transistors, starting with rGO film on Si/SiO_2 on which we evaporated 40nm thick interdigitated gold electrodes. Thanks to this configuration, we have individuated that source-drain current as function of a sweeping gate voltage always showed a shift toward positive voltages, with respect to the expected behavior, that prevented the Dirac point from being in the screened gate bias range. Seen the wide amplitude of the recorded curve, we supposed that the shift could be due to the high density of charged impurities either in the substrate or in proximity of the rGO film. Anyway, the device could act as sensor for nitrogen and water vapor. To shift the IV curve back to more negative voltages and possibly individuate the Dirac gate voltage, we doped the rGO films with Rhodamine 6G, which was previously known to negatively dope the graphene and to suffer from fluorescence quenching by the graphene itself. The resulting curves immediately after R6G drop-casting were right-shifted and the Dirac gate voltage was around 10V. Air exposure led to a decrease of the doping effect, with a shift of the Dirac gate voltage around 30V, while irradiation of the sample with

LED at 530nm (in correspondence of the absorbance peak of Rhodamine 6G) brought the V_g^D back to ~10V, as a result of the electron transfer during the quenching of the R6G fluorescence by graphene. This electron transfer could not be reversed by simply switching off the LED; we had instead to set the trapped electrons free repeating the measurement many times as to let the current flow through the channel.

Finally, we optimized a transfer method that allows to move the rGO film from the substrate necessary for the reduction. Etching the silicon oxide with warm KOH solution, we made the rGO film float in solution and we could fish it with the desired substrate. To avoid breaking the film, we protected it with a PMMA layer that could be removed with warm acetone with no risk for the film itself. We were able to transfer the film on PET substrate as to prove the flexibility of our transparent and conductive film, that show no meaningful decrease of the electric performances when bended. Moreover, we have also transferred the film onto a patterned Si/SiO_2 substrate as to have rGO film suspended over micrometric wells. Thanks to this configuration, we were able to measure the 2D Young modulus of the rGO film by AFM force spectroscopy and we have obtained values of the order of 10^3N/m, that is to say one order of magnitude higher than those reported for graphene.

Bibliography

[1] K. S. Novoselov, A. K. Geim, S. V. Morozov, D. Jiang, Y. Zhang, S. V. Dubonos, I. V. Grigorieva, and A. A. Firsov. Electric field effect in atomically thin carbon films. *Science (New York, N.Y.)*, 306(5696):666–669, 2004.

[2] T. Enoki, M. Endo, and M. Suzuki. *Graphite intercalation compounds and applications.* Oxford University Press, Oxford, 2003.

[3] A. K. Geim and K. S. Novoselov. The rise of graphene. *Nat. Mater.*, 6:183–191, 2007.

[4] S. V. Morozov, K. S. Novoselov, M. I. Katsnelson, F. Schedin, D. C. Elias, J. A. Jaszczak, and A. K. Geim. Giant intrinsic carrier mobilities in graphene and its bilayer. *Physical Review Letters*, 100(1):11–14, 2008.

[5] F. Schedin, A. K. Geim, S. V. Morozov, E. W. Hill, P. Blake, M. I. Katsnelson, and K. S. Novoselov. Detection of individual gas molecules adsorbed on graphene. *Nature materials*, 6(9):652–655, 2007.

[6] K. S. Kim, Y. Zhao, H. Jang, S. Y. Lee, J. M. Kim, K. S. Kim, J.-H. Ahn, P. Kim, J.-Y. Choi, and B. H. Hong. Large-scale pattern growth of graphene films for stretchable transparent electrodes. *Nature*, 457(7230):706–710, 2009.

[7] P. W. Sutter, J.-I. Flege, and E. A. Sutter. Epitaxial graphene on ruthenium. *Nature materials*, 7(5):406–411, 2008.

[8] W. S. Hummers and R. E. Offeman. Preparation of Graphitic Oxide. *J. Am. Chem. Soc*, 80(1937):1339, 1958.

[9] A. C. Ferrari and Et Al. Science and technology roadmap for graphene, related two-dimensional crystals, and hybrid systems. *Nanoscale*, 2014.

[10] M. Nasrollahzadeh, F. Babaei, P. Fakhri, and B. Jaleh. Synthesis,characterization, structural, optical properties and catalytic activity of reduced graphene oxide/copper nanocomposites. *RSC Adv.*, 5(14):10782–10789, 2015.

[11] C. Berger, X. Wu, N. Brown, C. Naud, X. Li, Z. Song, D. Mayou, T. Li, J. Hass, A. Marchenkov, E. H. Conrad, P. N. First, and W. A. De Heer. Electronic Confinement and Coherence in Patterned Epitaxial Graphene. *Science*, 312(May):1191–1196, 2006.

[12] J. Wintterlin and M. L. Bocquet. Graphene on metal surfaces. *Surface Science*, 603(10-12):1841–1852, 2009.

[13] T. A. Land, T. Michely, R. J. Behm, J. C. Hemminger, and G. Comsa. STM investigation of single layer graphite structures produced on Pt(111) by hydrocarbon decomposition. *Surface Science*, 264(3):261–270, 1992.

[14] M. Eizenberg and J. M. Blakely. Carbon monolayer phase condensation on Ni(111). *Surface Science*, 82(1):228–236, 1979.

[15] D. R. Dreyer, S. Park, C. W. Bielawski, and R. S. Ruoff. The chemistry of graphene oxide. *Chemical Society reviews*, 39(1):228–240, 2010.

[16] S. Pei and H. M. Cheng. The reduction of graphene oxide. *Carbon*, 50(9):3210–3228, 2012.

[17] H. C. Schniepp, J. L. Li, M.J. McAllister, H. Sai, M. Herrera-Alonson, D. H. Adamson, R. K. Prud'homme, R. Car, D. A. Seville, and I. A. Aksay. Functionalized single graphene sheets derived from splitting graphite oxide. *Journal of Physical Chemistry B*, 110(17):8535–8539, 2006.

[18] K. N. Kudin, B. Ozbas, H. C. Schniepp, R. K. Prud'homme, I. A. Aksay, and R. Car. Raman Spectra of Graphite Oxide and Functionalized Graphene Sheets. *Nano Letters*, 8(1):36–41, 2008.

[19] H. A. Becerril, J. Mao, Z. Liu, R. M. Stoltenberg, Z. Bao, and Y. Chen. Evaluation of Solution-Processed Reduced Graphene Oxide Films as Transparent Conductors. *ACS Nano*, 2(3):463–470, 2008.

[20] F. Wang. Gate-variable optical transitions in graphene. *Science*, 320:206–209, 2008.

[21] X. Li, H. Wang, J. T. Robinson, H. Sanchez, G. Diankov, and H. Dai. Simultaneous Nitrogen-Doping and Reduction of Graphene Oxide. pages 1–9, 2009.

[22] T. Szabó, O. Berkesi, P. Forgó, K. Josepovits, Y. Sanakis, D. Petridis, and I. Dékány. Evolution of surface functional groups in a series of progressively oxidized graphite oxides. *Chemistry of Materials*, 18(11):2740–2749, 2006.

[23] C. Hontoria-Lucas, A. J. López-Peinado, J. D. López-González, M. L. Rojas-Cervantes, and R. M. Martín-Aranda. Study of oxygen-containing groups in a series of graphite oxides: Physical and chemical characterization. *Carbon*, 33(11):1585–1592, 1995.

[24] D. Yang, A. Velamakanni, G. Bozoklu, S. Park, M. Stoller, R. D. Piner, S. Stankovich, I. Jung, D. A. Field, C. A. Ventrice, and R. S. Ruoff. Chemical analysis of graphene oxide films after heat and chemical treatments by X-ray photoelectron and Micro-Raman spectroscopy. *Carbon*, 47(1):145–152, 2009.

[25] C.-H. Chuang, Y.-F. Wang, Y.-C. Shao, Y.-C. Yeh, D.-Y. Wang, C.-W. Chen, J. W. Chiou, S. C. Ray, W. F. Pong, L. Zhang, J. F. Zhu, and J. H. Guo. The effect of thermal reduction on the photoluminescence and electronic structures of graphene oxides. *Scientific reports*, 4:4525, 2014.

[26] W. Gao, L. B. Alemany, L. Ci, and P. M. Ajayan. New insights into the structure and reduction of graphite oxide. *Nat Chem*, 1(5):403–408, August 2009.

[27] N. Yang, J. Zhai, D. Wang, Y. Chen, and L. Jiang. Two-dimensional graphene bridges enhanced photoinduced charge transport in dye-sensitized solar cells. *ACS Nano*, 4:887–894, 2010.

[28] G. Eda, G. Fanchini, and M. Chhowalla. Large-area ultrathin films of reduced graphene oxide as a transparent and flexible electronic material. *Nature nanotechnology*, 3(5):270–274, 2008.

[29] X. Wang, L. Zhi, and K. Mullen. Transparent, conductive graphene electrodes for dye-sensitized solar cells. *Nano Lett.*, 8:323–327, 2007.

[30] W.H. Lee, J. W. Suk, J. Lee, Y. Hao, J. Park, J. W. Yang, H. W. Ha, S. Murali, H. Chou, D. Akinwande, K. S. Kim, and R. S. Ruoff. Simultaneous transfer and doping of CVD-grown graphene by fluoropolymer for transparent conductive films on plastic. *ACS Nano*, 6(2):1284–1290, 2012.

[31] R. G. Gordon. Criteria for Choosing Transparent Conductors. *MRS Bulletin*, 25(08):52–57, 2000.

[32] A. Elschner, S. Kirchmeyer, W. Lovenich, U. Merker, and K. Reuter. *PEDOT: Principles and Applications of an Intrinsically Conductive Polymer*. 2010.

[33] R. L. Crabb and F. C. Treble. Thin Silicon Solar Cells for Large Flexible Arrays. *Nature*, 213(5082):1223–1224, March 1967.

[34] K. A. Ray. Flexible Solar Cell Arrays for Increased Space Power. *IEEE Trans Aerosp Electron Syst*, AES-3(1):107–115, 1970.

[35] B. C. Brodie. Sur le poids atomique du graphite. *Ann. Chim. Phys.*, 59:466–472, 1860.

[36] N. D. Young, G. Harkin, R. M. Bunn, D. J. McCulloch, R. W. Wilks, and a. G. Knapp. Novel fingerprint scanning arrays using polysilicon TFT's on glass and polymer substrates. *IEEE Electron Device Letters*, 18(1):19–20, 1997.

[37] P. M. Smith, P. G. Carey, and T. W. Sigmon. Excimer laser crystallization and doping of silicon films on plastic substrates. *Applied Physics Letters*, 70(3), 1997.

[38] J. a. Rogers, T. Someya, and Y. Huang. Materials and mechanics for stretchable electronics. *Science (New York, N.Y.)*, 327(5973):1603–1607, 2010.

[39] K. S. Novoselov and A. H. Castro Neto. Two-dimensional crystals-based heterostructures: materials with tailored properties. *Physica Scripta*, 2012(T146):14006, 2012.

[40] W. S. Wong and A. Salleo. *Flexible Electronics: Materials and Applications.* 2009.

[41] D. C. Marcano, D. V. Kosynkin, J. M. Berlin, A. Sinitskii, Z. Sun, Al. Slesarev, L. B. Alemany, W. Lu, and J. M. Tour. Improved Synthesis of Graphene Oxide. *ACS Nano*, 4(8):4806–4814, 2010.

[42] Graphenea. Product Datasheet Graphenea Graphene Oxide (GO).

[43] U. Brackmann. Lambdachrome Laser Dyes. *Lambdachrome Laser Dyes*, 3.:294, 2000.

[44] X. Zhou, S. He, K. A. Brown, J. Mendez-Arroyo, F. Boey, and C. A. Mirkin. Locally altering the electronic properties of graphene by nanoscopically doping it with rhodamine 6G. *Nano Letters*, 13(4):1616–1621, 2013.

[45] F. M. Zehentbauer, C. Moretto, R. Stephen, T. Thevar, J. R. Gilchrist, D. Pokrajac, K. L. Richard, and J. Kiefer. Fluorescence spectroscopy of Rhodamine 6G: Concentration and solvent effects. *Spectrochimica Acta - Part A: Molecular and Biomolecular Spectroscopy*, 121:147–151, 2014.

[46] K.-L. Fan, Z.-K. Guo, Z.-G. Geng, J. Ge, S.-L. Jiang, J.-H. Hu, and Q. Zhang. How Graphene Oxide Quenches Fluorescence of Rhodamine 6G. *Chinese Journal of Chemical Physics*, 26(3):252, 2013.

[47] H. Ren, D. D. Kulkarni, R. Kodiyath, W. Xu, I. Choi, and V. V. Tsukruk. Competitive adsorption of dopamine and rhodamine 6G on the surface of graphene oxide. *ACS Applied Materials and Interfaces*, 6(4):2459–2470, 2014.

[48] Y. Pang, Y. Cui, Y. Ma, H. Qian, and X. Shen. Fluorescence quenching of cationic organic dye by graphene: interaction and its mechanism. *Micro & Nano Letters*, 7(7):608, 2012.

[49] H. Chang, Z. Sun, Q. Yuan, F. Ding, X. Tao, F. Yan, and Z. Zheng. Thin film field-effect phototransistors from bandgap-tunable, solution-processed, few-layer reduced graphene oxide films. *Advanced Materials*, 22(43):4872–4876, 2010.

[50] L. Gross, F. Mohn, N. Moll, P. Liljeroth, and G. Meyer. The chemical structure of a molecule resolved by atomic force microscopy. *Science (New York, N.Y.)*, 325(5944):1110–4, August 2009.

[51] J. W. Steed and P. A. Gale. *Supramolecular Chemistry: From Molecules to Nanomaterials.* 2012.

[52] R. Hoffmann, A. Baratoff, H. J. Hug, H. R. Hidber, H. V. Löhneysen, and H.-J. Güntherodt. Mechanical manifestations of rare atomic jumps in dynamic force microscopy. *Nanotechnology*, 18(39):395503, 2007.

[53] T. Ando, T. Uchihashi, and T. Fukuma. High-speed atomic force microscopy for nano-visualization of dynamic biomolecular processes. *Progress in Surface Science*, 83(7-9):337–437, 2008.

[54] P. Eaton and P. West. Atomic Force Microscopy. *Physical review letters*, 2010.

[55] J. M. Balthazar, A. M. Tusset, A. M. Bueno, and B. Rodrigues de Pontes. *Nonlinearity, Bifurcation and Chaos - Theory and Applications.* InTech, October 2012.

[56] C. A. J. Putman, K. O. Van der Werf, B. G. De Grooth, N. F. Van Hulst, and J. Greve. Tapping mode atomic force microscopy in liquid. *Applied Physics Letters*, 64(18):2454, May 1994.

[57] Thermo Scientific. *K-Alpha: A New Concept in XPS.* 2008.

[58] P. Van der Heide. *X-ray Photoelectron Spectroscopy: An introduction to Principles and Practices*, volume 2011. 2011.

[59] C. Wargo and PChem Associates. Characterization of Conductors for Printed Electronics. *White Papers*, pages 1–12.

[60] L.B. Valdes. Resistivity Measurements on Germanium forTransistors. *Procedings of the I.R.E.*, 29:420–427, 1954.

[61] P. Ceroni. *The Exploration of Supramolecular Systems and Nanostructures by Photochemical Techniques: Exploration of Supramolecular Systems and Nanostructures By Photochemical Techniques.* Springer, 2011.

[62] RKI Instruments. Photoelectron spectroscopy.

[63] M. Uda, Y. Tomioka, C. Kouno, H. Ishida, and Y. Yamauchi. Open counter for low energy electron detection with suppressed background noise, 1989.

[64] P. J. Haines. *Principles of Thermal Analysis and Calorimetry.* 2002.

[65] P. Gabbott. *Principles and applications of thermal analysis.* 2008.

[66] M. Wagner. Thermal Analysis in Practice in Practice.

[67] X. Li. Highly conducting graphene sheets and Langmuir-Blodgett films. *Nature Nanotechnol.*, 3:538–542, 2008.

[68] M. J. McAllister, J.-L. Li, D. H. Adamson, H. C. Schniepp, A. A. Abdala, J. Liu, O. M. Herrera-alonso, D. L. Milius, R. Car, R. K. Prud, and I. A. Aksay. Single Sheet Functionalized Graphene by Oxidation and Thermal Expansion of Graphite. *Society*, 19(4):4396–4404, 2007.

[69] S. M. Song, J. K. Park, O. J. Sul, and B. J. Cho. Determination of work function of graphene under a metal electrode and its role in contact resistance. *Nano Letters*, 12(8):3887–3892, 2012.

[70] A. Shaffique, E. H. Hwang, V. M. Galitski, and S. Das Sarma. A self-consistent theory for graphene transport. *Proceedings of the National Academy of Sciences of the United States of America*, 104(47):18392–18397, 2007.

[71] J. Lu. One-pot synthesis of fluorescent carbon nanoribbons, nanoparticles, and graphene by the exfoliation of graphite in ionic liquids. *ACS Nano*, 3:2367–2375, 2009.

[72] I. Jung, D. Dikin, S. Park, W. Cai, S. L. Mielke, and R. S. Ruoff. Effect of Water Vapor on Electrical Properties of Individual Reduced Graphene Oxide Sheets Effect of Water Vapor on Electrical Properties of Individual Reduced Graphene Oxide Sheets. 300:20264–20268, 2008.

[73] J. T. Robinson, M. Zalalutdinov, J. W. Baldwin, E. S. Snow, Z. Wei, P. Sheehan, and B. H. Houston. Wafer-scale reduced graphene oxide films for nanomechanical devices. *Nano Letters*, 8(10):3441–3445, 2008.

[74] C. Lee, X. Wei, J. W. Kysar, and J. Hone. Measurement of the elastic properties and intrinsic strength of monolayer graphene. *Science (New York, N.Y.)*, 321(5887):385–388, 2008.

[75] O. L. Blakslee, D. G. Proctor, E. J. Seldin, G. B. Spence, and T. Weng. Elastic Constants of Compression-Annealed Pyrolytic Graphite. *Journal of Applied Physics*, 41:3373, 1970.